Using observational mean-flow data to drive large-eddy simulations of a diurnal cycle at the SWiFT site

Allaerts, Dries; Quon, Eliot; Churchfield, Matt

DOI
10.1002/we.2811

Publication date
2023

Document Version
Final published version

Published in
Wind Energy

Citation (APA)
Allaerts, D., Quon, E., & Churchfield, M. (2023). Using observational mean-flow data to drive large-eddy simulations of a diurnal cycle at the SWiFT site. *Wind Energy*, *26*(5), 469-492. https://doi.org/10.1002/we.2811

Received: 19 September 2022 | Revised: 23 December 2022 | Accepted: 25 January 2023

DOI: 10.1002/we.2811

RESEARCH ARTICLE

WILEY

Using observational mean-flow data to drive large-eddy simulations of a diurnal cycle at the SWiFT site

Dries Allaerts[1] | Eliot Quon[2] | Matt Churchfield[2]

[1]Faculty of Aerospace Engineering, Delft University of Technology, Delft, The Netherlands

[2]National Wind Technology Center, National Renewable Energy Laboratory, Golden, Colorado, USA

Correspondence
Dries Allaerts, TU Delft, Kluyverweg 1, 2629 HS Delft, The Netherlands.
Email: D.J.N.Allaerts-1@tudelft.nl

Abstract

Reproducing realistic date- and site-specific unsteady wind conditions in large-eddy simulations is becoming increasingly useful in wind energy. How to run a large-eddy simulation to match observed conditions, however, remains an open research question. One approach that has received considerable attention is mesoscale-to-microscale coupling, in which information about the mesoscale weather, most commonly acquired from a mesoscale numerical weather model, is passed on to a microscale model. In this paper, we demonstrate how the recently developed profile-assimilation technique, a form of mesoscale-to-microscale coupling, can be used to drive large-eddy simulations solely based on observed mean-flow profiles at a single location, bypassing the need for auxiliary mesoscale simulations. The new approach is evaluated for a diurnal cycle at the Scaled Wind Farm Technology site. Observed mean-flow profiles from the ground up to a height of 2 km are reconstructed by aggregating measurements from multiple instruments, and gaps in the data are infilled with natural neighbor interpolation. We perform nine simulations using various forcing approaches to deal with data limitations. The results show that it is indeed possible to drive microscale large-eddy simulation with observations using the profile-assimilation technique, notwithstanding large gaps in virtual potential temperature measurements. However, profile assimilation with vertical smoothing of the error between the desired and actual profiles is required. Without that smoothing, the microscale simulations develop unrealistically high turbulence levels under many situations. Finally, we show that simulated mesoscale data can account for missing observations, although care is needed as both data sources are not necessarily compatible.

KEYWORDS

afternoon/evening transition, atmospheric boundary layer, diurnal cycle, large-eddy simulation, low-level jet, mesoscale-to-microscale coupling, profile assimilation

Abbreviations: ABL, atmospheric boundary layer; DPA, direct profile assimilation; IPA, indirect profile assimilation; LES, large-eddy simulation; LLJ, low-level jet; MMC, mesoscale-to-microscale coupling; NWP, numerical weather prediction; RASS, radar acoustic sounding system; TKE, turbulent kinetic energy; TTU, Texas Tech University; WRF, Weather Research and Forecasting.

1 | INTRODUCTION

There is a growing need for detailed, date- and site-specific information on unsteady wind conditions for wind energy use cases like wake flow analysis, high- and low-fidelity model development and validation, and testing of wind farm control strategies, to name a few. Field observations present a logical source of information, but there is often a trade-off between overall spatial extent and spatio-temporal resolution. For example, meteorological towers can measure high-frequency data (a typical sensor sampling rate is 50 Hz), but their spatial extent is inherently one-dimensional and limited by the height of the tower. Lidars, on the other hand, can cover a larger spatial extent, but to cover two-dimensional or three-dimensional measurement areas, they need time to complete scanning patterns, and the spatial measurements therefore have a low effective temporal resolution. In light of these limitations, large-eddy simulations (LES) can provide a useful means of augmenting field observations with high-resolution, three-dimensional and time-varying turbulent flow data.

One of the challenges in augmenting field observations with LES is how to run the simulation such that it matches the observed conditions. In some cases, the microscale flow (i.e., considering flow phenomena with length scales less than 3 km[1]) is horizontally homogeneous to a good approximation so that the flow can be simulated using a doubly periodic simulation domain. This way, no inflow or outflow boundary conditions are needed, thus avoiding the need to specify turbulent inflow conditions. In such a doubly periodic simulation setup, the input required to numerically reproduce the observed wind conditions then includes initial conditions, surface boundary conditions, and large-scale forcing data. The latter is needed to incorporate the effect of mesoscale meteorological variability, which is typically not represented explicitly by the microscale model, and involves terms such as the pressure-gradient force and large-scale advection of momentum and temperature.

There are various ways to set the large-scale forcing data. The simplest approach is to assume canonical conditions, like a time- and height-independent pressure gradient and no large-scale advection. The magnitude of the pressure gradient and the surface boundary condition is thereby selected to match a number of key flow parameters, such as wind speed and turbulence intensity at a particular reference height. This approach was used in the well-known GABLS1 intercomparison study (Global Energy and Water Cycle Experiment (GEWEX) Atmospheric Boundary Layer Study).[2] An example of its use in a wind energy application can be found in a recent validation study comparing LES with field measurements obtained from the Lillgrund offshore wind farm.[3] Some studies add slightly more detail such as a constant subsidence rate[4] or a prescribed time and/or height dependence of the geostrophic pressure gradient.[5]

Another approach to obtain large-scale forcing data would be to rely on observations. However, quantities like large-scale advective tendencies and subsidence cannot be observed directly from field measurements, so they need to be derived from other field observations instead. One way is to use a wind profiler and/or radiosonde network to obtain a synoptic description of the large-scale dynamical and thermodynamic fields, which can then be differentiated to yield wind divergence and horizontal gradients. This approach was used, for example, in the Atmospheric Radiation Measurement (ARM) program of the U.S. Department of Energy.[6,7] The main disadvantage of this approach is that it relies on a high-density network of observations, which is often not available or only available for a limited amount of time during a specific intensive operational period. Moreover, the uncertainty in horizontal gradients derived from such a network can easily be as large as the expected synoptic-scale signal itself.[8] Alternatively, dynamical tendencies could also be derived from the vertical divergence of turbulent fluxes along a single tower.[9] However, the divergence is usually quite small and hence difficult to measure accurately, and the approach also suffers from practical issues related to local-scale advection.[10]

A third approach relies on mesoscale data generated from a numerical weather prediction (NWP) model. Most studies directly apply large-scale forcing extracted from the NWP model,[11–18] although some modify the numerical forcing based on observations before applying them in the microscale simulation.[10,19] A downside of this approach is that the numerical estimate of the large-scale forcing is sensitive to the NWP's resolution and physical parametrization.[10,12,20] As an alternative, a number of studies account for the larger-scale atmospheric variability implicitly by applying some form of Newtonian relaxation data assimilation technique to incorporate NWP vertical soundings into the microscale simulations.[21–25] Finally, some studies combine NWP modeling with available observations by applying observational nudging at the mesoscale[26,27] or the microscale level.[28] However, downsides to nudging are that it introduces modeling complexity and uncertainty in the nudging parameters (nudging weight, spatial projection, and temporal filter). Despite the many different approaches found in literature, there is a need for a robust way to directly impose observations in microscale simulations.

We propose a new approach to drive LES based on observational data from a single location using the profile-assimilation technique recently developed by Allaerts et al.[25] (hereafter A20). This technique was originally intended as a mesoscale-to-microscale coupling (MMC) method to drive microscale LES with time–height profiles of mean-flow quantities generated by a mesoscale model, and it has been used for both onshore[25,29] and offshore conditions.[30,31] Profile assimilation can be applied directly (acting at every vertical grid level) or indirectly (applying vertical smoothing), and it is was shown in A20 that the indirect profile assimilation (IPA) technique is a viable alternative to the approach based on mesoscale budget components,[28] as described in the previous paragraph. In this study, we replace the mesoscale-model-generated time–height profiles with observational data. The main advantage of this approach is that it is independent from auxiliary mesoscale simulations and that it does not require extensive measurement campaigns. We address the following research questions related to the use of profile assimilation with observational data:

(i) Is it possible to drive large-eddy simulations with observational data rather than using mesoscale-model output?
(ii) Is observational data accurate enough to enable the use of direct profile assimilation (i.e., without vertical smoothing)?
(iii) Can mesoscale-model output be used to fill in gaps present in the observational data used to drive LES?

Throughout this study, we focus on the diurnal cycle observed on November 8 and 9, 2013, at the Scaled Wind Farm Technology (SWiFT) facility in West Texas. The U.S. Department of Energy's (DOE's) Atmosphere to Electrons (A2e) MMC project identified this particular day as a representative diurnal cycle over flat terrain with relevance for wind energy application,[32] and the case has been used in several studies to validate MMC techniques.[25,33] The SWiFT site is equipped with a wide variety of meteorological measurement facilities hosted by the National Wind Institute at Texas Tech University (TTU), including a 200-m meteorological tower and a boundary-layer radar profiler. For more details about the SWiFT site and the measurement facilities, the reader is referred to the relevant technical reports about the SWiFT site.[34,35]

The remainder of the paper is organized as follows. The various sources of observational data and the way that data gaps are infilled to form a continuous time–height history of wind and temperature are described in Section 2. Next, Section 3 explains the simulation methodology and numerical setup, and gives an overview of the various simulations performed in this study. The results are discussed in Section 4, and conclusions are drawn in Section 5.

2 | OBSERVATIONAL DATA

We compile data from three different data sources to form a continuous time–height history of wind and temperature to use as forcing in our SWiFT diurnal case study. The TTU 200-m meteorological tower is instrumented with sonic anemometers along with temperature, relative humidity, and barometric pressure probes at 10 different height levels between 0.9 and 200.0 meters above ground level (AGL).[35] To obtain near-surface winds, the 50-Hz sonic-anemometer data are transformed to remove tilt-misalignment errors, then averaged to obtain 10-min mean wind speed and direction. We choose to employ time-averaged rather than instantaneous data to calculate the large-scale forcing so as not to affect turbulence directly, and the 10-min timescale is chosen based on standard practices in wind engineering and for consistency with prior work.[25]

Even though this meteorological tower is taller than typically deployed towers, the wind and temperature measurements do not reach the top of a typical computational fluid dynamics (CFD) domain for a microscale simulation. We therefore supplement the sonic anemometer measurements with scans from a nearby radar profiler provided by TTU.[†] Two scan modes with overlapping ranges are employed: a short-range scan ("type 0") ranging from 150 to 2000 m AGL, with approximately 60-m resolution; and a long-range scan ("type 1") from 600 to 6000 m, with approximately 200-m resolution. Data were recorded at 20-min intervals. All scan data with signal-to-noise ratio (SNR) below −22.5 dB are excluded; this threshold value is selected by looking at profiles of SNR and selecting a cutoff that excluded SNR minima for the duration of the study period. After the quality control step, we resample the radar data to 10-min intervals using linear interpolation to match with the tower data. A full wind data set is formed by aggregating all wind measurements (see left column of Figure 1), including point measurements from the meteorological tower and radar measurements that represent a volume average within each range gate. To infill the excluded data in the full data set, a natural neighbor algorithm is applied, which applies volume-weighted interpolation to produce a smoothly varying field (see right column of Figure 1).

A similar approach is applied to the virtual temperature profiles from the radar acoustic sounding system (RASS). However, unlike the wind profiles, only a single scan type is used and radar-measured virtual temperature data are not available above 550 m AGL (see Figure 2 on the left). Extensive data gaps below 550 m make interpolation impossible. To supplement the RASS data, we collect radiosonde data available at 12-h intervals from nearby National Weather Service (NWS) launch sites at Amarillo and Midland airports, both about 185 km away from the SWiFT site. Given that SWiFT is at the midpoint between the two sounding locations, we take the local atmospheric profiles to be the average of the two sites. Near-surface virtual temperature profiles are calculated from temperature, pressure, and relative humidity measurements from the meteorological mast. To account for local flow effects, the mean sounding profile is shifted such that the sounding and met-mast temperatures are in agreement at the top of the met mast. This shift retains the ABL structure in the free atmosphere from the sounding, while providing a smooth transition from local measurements near the surface to distant measurements aloft—otherwise, a discontinuity in the temperature profiles at the top of the met mast could introduce unphysical thermal stratification effects. Virtual temperatures are converted to virtual potential temperature by further assuming that the full pressure profile can be modeled by the hypsometric equation, with the scale height estimated from the pressure probes on the meteorological tower. Finally, the resulting temperature data are infilled with natural neighbor interpolation, as shown in Figure 2 on the right.

[†]Despite the meteorological tower and radar profiler being located about 540 m apart,[34] we will assume that the measurement facilities are co-located. The rationale is that we are only interested in observed mean-flow quantities, and our assumption of horizontal homogeneity implies that at both locations one would observe the same mean-flow profiles.

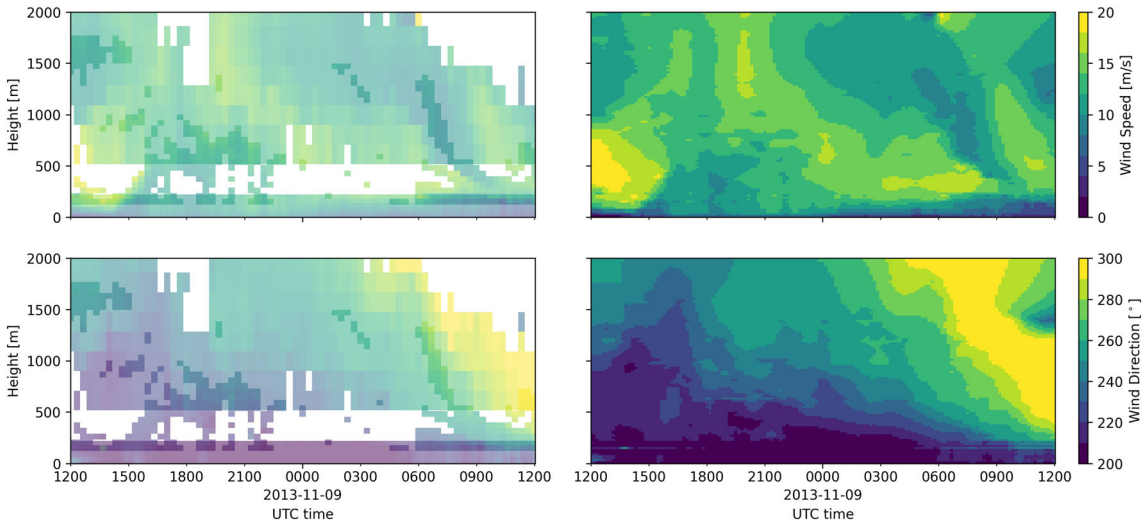

FIGURE 1 Observed time–height history of horizontal wind speed (top) and wind direction (bottom): Overlaid measurements from the meteorological tower and two radar profiler scan modes (left); measurements with data gaps infilled using natural neighbor interpolation (right)

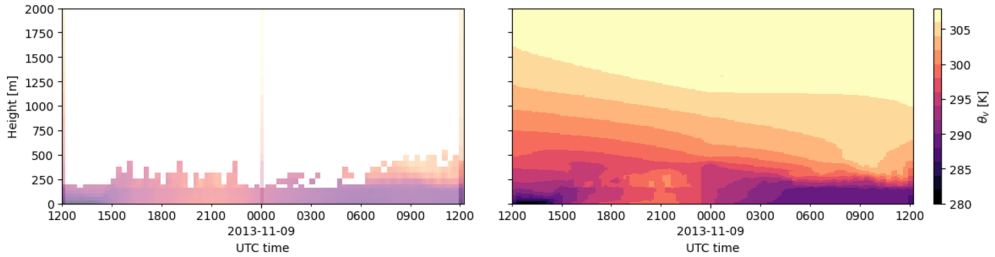

FIGURE 2 Observed time–height history of virtual potential temperature: Overlaid measurements from the meteorological tower, the radar acoustic sounding system, and sounding data from nearby airports (left); measurements with data gaps infilled using natural neighbor interpolation (right)

3 | SIMULATION METHODOLOGY AND NUMERICAL SETUP

We perform a suite of microscale large-eddy simulations with the aim to accurately reproduce the turbulent wind conditions observed during the SWiFT diurnal cycle case. In general, to simulate realistic wind conditions at the microscale level, detailed information is needed about the initial conditions, boundary conditions, and possibly other sources of momentum or energy not represented in the microscale simulation. However, in light of the relatively simple geographical and meteorological conditions during the SWiFT diurnal cycle case, we will assume that the flow conditions at the microscale level are homogeneous in the horizontal directions. The assumption of horizontal homogeneity allows the use of a doubly periodic simulation domain, avoiding the need for inflow/outflow boundary conditions and inflow perturbations, which would otherwise be required to initiate resolved turbulence. In the doubly periodic simulation setup, the main drivers of the microscale flow are surface boundary conditions and horizontally homogeneous, time–height-varying volumetric forcing terms, which account for the impact of mesoscale processes like large-scale advection or synoptic pressure distributions. In this study, we explore various methods to estimate these large-scale forcing terms based on observational data.

3.1 | Large-scale forcing methodology

The horizontally homogeneous, time–height-varying large-scale forcing terms required to drive the microscale simulation are obtained using the profile-assimilation technique.[25] This technique takes as input the time–height history of mean-flow quantities like velocity and virtual potential temperature (from either observations or mesoscale simulations) and outputs an estimate of the force of the underlying physical large-scale processes that lead to the given mean-flow time–height history. The forcing terms are computed as the microscale solution progresses forward in

time, and applied to the transport equations for momentum and virtual potential temperature of the microscale simulation. We use two different algorithms to estimate the forcing terms: direct profile assimilation (DPA) and indirect profile assimilation (IPA).

DPA consists of a simple proportional gain controller that relates the large-scale forcing term F_φ to the error e_φ between the input profile and the simulated microscale mean-flow profile: $F_\varphi(t,z) = K_p e_\varphi(t,z)$ where $e_\varphi(t,z) = \varphi_{\text{input}}(t,z) - \varphi_{\text{LES}}(t,z)$ and where φ represents one of the horizontal wind components or the virtual potential temperature. The microscale mean-flow profile $\varphi_{\text{LES}}(t,z)$ is computed by averaging over horizontal planes so as to filter out resolved turbulent fluctuations. Following A20, the gain K_p is set to 0.2 s^{-1}. The horizontally homogeneous large-scale forcing is applied in every grid cell throughout the entire numerical domain. The fact that these forcing terms are calculated at every vertical level and at every instant in time independently implies that DPA does not impose any time dependency or vertical correlation on the large-scale forcing. It has been found before that this lack of spatial and temporal correlation in the forcing terms may affect the resolved turbulence levels,[25] and in this study, we will investigate whether that also holds when using observational data as input (see also § 3.2).

IPA is a modified version of DPA that aims to constrain the vertical variability of the calculated forcing terms by correlating the controller actions at different vertical levels. This is achieved by providing the proportional gain controller with a polynomial fit of the vertical error profile $\tilde{e}_\varphi$ rather than the actual error profile e_φ. The polynomial fit thereby introduces a form of vertical smoothing or low-pass filtering. We employ the baseline configuration of A20, which applies a cubic polynomial fit with uniform weights. Similar to DPA, the controller gain for IPA is set to $K_p = 0.2\ s^{-1}$.

It is important to note that both DPA and IPA apply horizontally homogeneous forcing terms throughout the entire simulation domain, and we only use 10-min averages for the input profiles (input data is available at a sampling rate of 10 min and we use linear interpolation to obtain input profiles at intermediate time steps). The forcing terms, therefore, affect the mean flow and do not directly impose turbulent fluctuations. Instead, all turbulent fluctuations in the microscale domain exist as a result of the forced mean conditions.

3.2 | Overview of simulations

We perform a total of nine large-eddy simulations of the SWiFT diurnal cycle using various forcing methods and data sources. Table 1 lists all simulations and details the applied forcing methodology. The suite of simulations can be subdivided into three distinct sets and one reference simulation.

All simulations except the reference make use of the velocity measurements from the meteorological tower and radar profiler to drive the momentum equations, and the simulations differ in terms of forcing method and data source for the virtual potential temperature as further explained below.

The first set of simulations (cases A0/1/n) uses the indirect profile assimilation method for momentum forcing. To deal with the limited availability of and the higher uncertainty associated with virtual potential temperature measurements, we perform three simulations employing one of the following methods for virtual potential temperature forcing (θ_v-forcing). First, case A0 does not apply θ_v-forcing at all and assumes that large-scale temperature advection is relatively small compared to other microscale processes, and that the diurnal forcing of the virtual potential temperature budget is mainly driven by surface heating and cooling. This approach removes the need for reliable temperature data other than surface measurements. Second, case A1 estimates the θ_v-forcing at a single height and then assumes that the large-scale forcing is constant with height. The benefit of this approach is that it allows us to use high-quality temperature and pressure measurements from a meteorological tower and

TABLE 1 Overview of simulations, respective methods used to account for large-scale forcing of momentum and virtual potential temperature, and objectives.

	Momentum forcing		Virtual potential temperature (θ_v) forcing		
Name	Method	Data source	Method	Data source	Objectives
A0	IPA	Tower + radar profiler	None	–	*Demonstrate the potential to drive LES with observational data*
A1	IPA	Tower + radar profiler	Single height	Tower at 74.7 m	
An	IPA	Tower + radar profiler	IPA	Tower + RASS + sounding	
B0	DPA	Tower + radar profiler	None	–	*Assess applicability of DPA in combination with observations*
B1	DPA	Tower + radar profiler	Single height	Tower at 74.7 m	
Bn	DPA	Tower + radar profiler	DPA	Tower + RASS + sounding	
Ca	IPA	Tower + radar profiler	IPA	Mesoscale model (WRF)	*Evaluate ability of WRF to replace missing data*
Cb	IPA	Tower + radar profiler	BC	Mesoscale model (WRF)	
R	IPA	Mesoscale model (WRF)	IPA	Mesoscale model (WRF)	*Reference case*

Note: The forcing methods are abbreviated as follows: IPA, indirect profile assimilation; DPA, direct profile assimilation; BC, budget components.

does not require measurements at higher altitudes. Similar to the "full" profile assimilation algorithms, the forcing is calculated as $F_{\theta_v}(t) = K_p e_{\theta_v}(t)$, and we set a higher gain value of $K_p = 2s^{-1}$. Third, case An uses IPA at all heights and therefore relies on complete time–height profiles. These are obtained by combining tower, RASS, and sounding data (see Section 2).

The second set of simulations (cases B0/1/n) is composed in the same way as the first set but uses direct profile assimilation. This set is included for the following reason. In A20, it was found that using DPA for mesoscale-to-microscale coupling strongly overpredicted turbulent kinetic energy (TKE) during the daytime of the SWiFT diurnal cycle, and they showed that DPA failed partly because of inaccuracies in the mesoscale profiles that were used as input to the algorithm. Here we use observational data rather than results from a mesoscale model. Assuming that input profiles based on observational data are more accurate, this second set of simulations investigates whether DPA can be used effectively in combination with observations.

The third set of simulations (cases Ca/b) consists of hybrid simulations combining observational data for momentum forcing and numerical data for virtual potential temperature forcing. The idea here is to see whether incomplete observational data sets can be complemented with numerical data from a mesoscale model. For the SWiFT diurnal cycle case in particular, complete time–height profiles of virtual potential temperature could only be composed by including sounding data from distant meteorological stations, so this third set is used to investigate whether θ_v-forcing based on observational data can be replaced by the more traditional MMC approach using mesoscale data from NWP alone. Simulation Ca uses θ_v-forcing based on IPA with time–height mesoscale profiles, and simulation Cb uses physics-based source terms extracted directly from the mesoscale governing equations (the so-called budget components approach[28,33]).

Finally, we also perform a reference simulation (case R) driven with data from a mesoscale model to compare the observations-driven approach presented in the current study with the more traditional mesoscale-model-driven approach. Case R uses IPA for both momentum and virtual potential temperature forcing. The time–height profiles are obtained from a mesoscale simulation using the National Center for Atmospheric Research's Weather Research and Forecasting (WRF) model (model configuration described in Appendix A1).[36] The simulation was performed in the context of a formal coupling comparison study initiated under the DOE's A2e MMC project.[37] The same WRF simulation is used to provide input for the θ_v-forcing for cases Ca and Cb.

3.3 | Numerical model and setup

The mesoscale-driven, microscale flow at the SWiFT site is simulated using NREL's microscale solver "Simulator fOr Wind Farm Applications" (SOWFA).[38,39] SOWFA is an incompressible large-eddy simulation code built upon the Open-source Field Operations And Manipulations (OpenFOAM) CFD toolbox. The code solves the conservation equations of mass, momentum, and potential temperature. Moisture is not explicitly accounted for by the solver. However, by using external forcing and initial conditions based on the virtual potential temperature, we are in fact solving the conservation equation for the virtual potential temperature (in the absence of phase changes). This way, we at least partially capture the impact of moisture on the microscale flow as the buoyancy force in the momentum transport equation takes into account the virtual potential temperature. Further, we use a standard prognostic subgrid-scale TKE model[40] to calculate the effect of the subgrid-scale motions on the resolved flow, and buoyancy is accounted for by means of the Boussinesq approximation.

The simulations are run on a horizontally periodic domain of $5 \times 5 \times 2$ km with a uniform grid resolution of 10 m in each direction, and they cover a period of 24 h with a fixed time step of 0.5 s. The simulations are initialized on 8 November 2013 at 1200 UTC (corresponding to 6 a.m. local time) using the observed vertical profiles of velocity and virtual potential temperature (case R is initialized with a WRF profile instead). Small amplitude periodic perturbations were superimposed on the velocity profile near the surface to accelerate the development of turbulence. In previous work we found that it only takes about 1 h to spin-up turbulence,[33] so we did not simulate any additional spin-up time. At the surface a standard wall stress and heat flux model is applied,[41,42] assuming a uniform surface roughness length of 0.1 m. The surface potential temperature, which is required for the surface heat flux model, is deduced from the potential temperature and the turbulent heat flux measured at the lowest station of the TTU meteorological tower using Monin–Obukhov similarity theory[1] (case R uses the surface potential temperature from WRF instead). Other boundary conditions include slip and a fixed temperature gradient at the top, and periodic boundary conditions on all lateral sides.

To enable a fair comparison with the point measurements from the meteorological tower, we use simulation data extracted along a single virtual tower in the middle of the numerical domain, and we do not exploit the periodicity of the numerical domain to apply horizontal averaging. The resolved turbulent stress tensor and heat flux are calculated based on turbulent fluctuations with respect to time-averaged quantities, using an averaging window of 10 min.

4 | RESULTS

The discussion of the results is organized in line with the research questions presented in the introduction. First, we analyze whether observational data alone can be used to drive large-eddy simulations of a diurnal cycle using indirect profile assimilation in Section 4.1 based on simulation

set A (see Table 1). Next, we use simulation set B in Section 4.2 to assess whether direct profile assimilation can be used in combination with observations. In Section 4.3, we determine whether mesoscale data can be used to fill in the gaps in the time–height profiles of virtual potential temperature, for which we use simulation set C. In these first three sections, we focus on the flow physics of the atmospheric boundary layer. Then, in Section 4.4, we discuss overall performance metrics of specific interest to wind energy.

4.1 | Data-driven LES using indirect profile assimilation

In this section, we focus on simulation set A in which momentum is forced using indirect profile assimilation and potential temperature is forced using a variety of forcing methods. The results of cases A0, A1, and An are compared with case R, which follows the more traditional mesoscale-to-microscale coupling approach based on data from a mesoscale model. We first consider the temporal evolution of the flow throughout the diurnal cycle in Section 4.1.1. Next, we focus on the vertical structure of the boundary layer in Section 4.1.2, and we look at some turbulence characteristics in Section 4.1.3.

4.1.1 | Diurnal evolution of the flow

We start with an overall impression of the diurnal evolution of the flow in Figure 3, showing the time–height contours of horizontal wind speed, wind direction, virtual potential temperature gradient, and TKE for the microscale simulations A0, A1, An, and R.

The last two columns show the time–height profiles obtained from observations (after gap filling with natural neighbor interpolation, see Section 2 and Figures 1 and 2) and from a mesoscale model (used to drive case R). Note that the observed TKE is only shown for reference and was not used to drive the simulations. To aid interpretation of the vertical structure, estimates of the height of the atmospheric boundary layer (ABL) are included. For convective conditions, the ABL height is taken as the vertical level where the turbulent heat flux is minimal, whereas for stable conditions we use the height at which the turbulent shear stress vanishes.[43] Further, sunrise (7:12 a.m. or 1312 UTC) and sunset (5:49 p.m. or 2349 UTC) are indicated by vertical dashed lines.

In terms of the horizontal wind speed and wind direction (top two rows of Figure 3), we observe that in general, all microscale simulations capture similar flow events throughout the diurnal cycle: After sunrise, the boundary layer grows rapidly in height, and it decreases again during the afternoon/evening transition;[‡] the wind speed and wind direction are well-mixed throughout the boundary layer during the daytime; and after sunset the wind speed increases due to an inertial oscillation triggered by the decay of turbulence. Taking a closer look reveals that there are also a number of clear differences between the various microscale simulations. First, case R shows the formation of a strong and narrow low-level jet (LLJ) at nighttime, whereas the LLJ is much broader in cases A0/1/n, which are driven by observations. Second, the evolution of the boundary-layer height is much smoother in case R compared to the other cases, which show some unusual behavior around sunrise and/or during the nighttime. We believe this erratic behavior is due to the difficulty of estimating the boundary-layer height from turbulent flux profiles under realistic atmospheric conditions. Further research is needed to understand why the boundary-layer height estimate is particularly sensitive for cases A0/1/n and less so for case R. Third, the time when the boundary layer height decreases from its daytime maximum also varies considerably among the various cases, which may indicate differences in the timing of the afternoon transition. Note also that the wind speed and wind direction in case R show a slightly different behavior near the top of the domain toward the end of the diurnal cycle compared to cases A0/1/n; that is, the wind speed decreases to low values and the wind direction turns clockwise to north and even northeast (360° and 60°, both out of range on the colormap so not shown). The trends in the wind speed in case R are in line with the corresponding input data from the WRF mesoscale simulation but the turning of the wind direction is overpredicted and might be due to a runaway effect of the IPA technique.[25] Finally, it is interesting to take a look at the last two columns as well, which represent the time–height profiles that were used to drive the data. Already in these input profiles large differences can be seen — for example, in the strength and width of the LLJ.

The third row of Figure 3 shows the vertical gradient of the virtual potential temperature, which is useful to visualize the vertical structure of the ABL.[§] In all simulations, we observe the rising of an entrainment zone (marked by a strong positive temperature gradient) during the daytime, and below this entrainment zone a well-mixed layer develops (marked by zero temperature gradient). At the surface, a thin region with negative virtual potential temperature gradients can be seen, which is characteristic for the daytime convective boundary layer and is caused by surface heating. During the daytime, the entrainment zone marks the top of the ABL, and here we again see that there are considerable differences in the height of the ABL among the various microscale simulations. Around sunset, the entrainment zone stops rising and stays at about the same height throughout the night. Note that the (processed) observational data show very little resemblance with the microscale simulation results and with

[‡]The terminology used in literature to indicate the boundary-layer transition from a daytime convective state to a nighttime stable state is somewhat ambiguous.[44] In this study, we use the term evening transition when referring to events occurring around or after sunset, while afternoon transition is used to indicate the period following solar noon when the heat-flux is decreasing.
[§]The idea to use the vertical gradient of the virtual potential temperature to visualize the vertical structure of the ABL was inspired by the work of Angevine et al.[44]

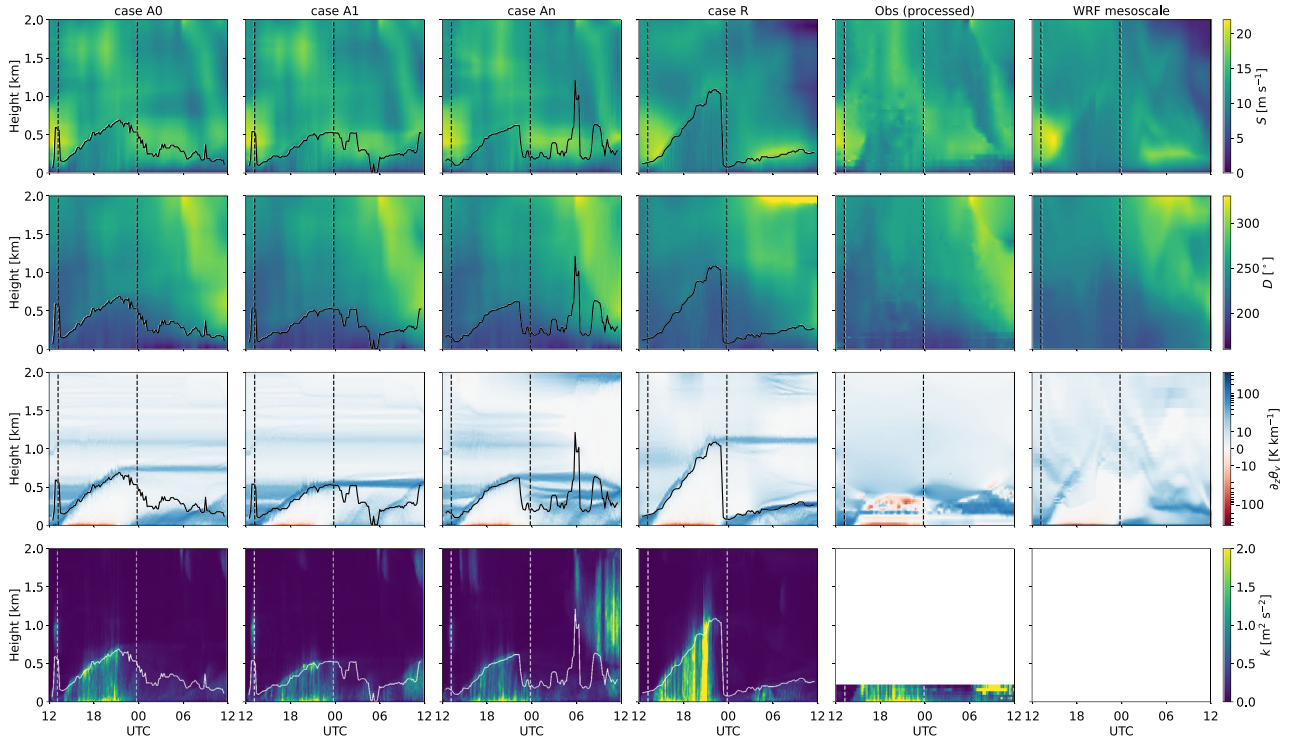

FIGURE 3 Time–height contours of horizontal wind speed S (first row), wind direction D (second row), virtual potential temperature gradient $\partial_z\theta_v$ (third row), and turbulent kinetic energy k (last row), for microscale simulations A0, A1, An, and R. The last two columns show observational data (all preprocessed except for TKE) and WRF mesoscale data for reference. All data correspond to 10-min averages. Solid lines show the estimated boundary layer height (rolling average of 1 h) and vertical dashed lines indicate sunrise and sunset.

the reference mesoscale simulation in terms of the virtual potential temperature gradient (see, e.g., the discontinuity near the top of the met-mast during the daytime), which calls in to question the quality of the virtual potential temperature data processing. Moreover, the information appears to be limited to the lowest 500 m, and there is no clear sign of an entrainment zone rising above the daytime boundary layer. The lack of information higher up is maybe not surprising in light of Figure 2, which shows that the only source of virtual potential temperature measurements at these heights were radiosonde data at 12-h intervals. To obtain better estimates of the θ_v-forcing, we would need accurate profile measurements up to greater altitudes, at higher frequency.

Lastly, time–height profiles of turbulent kinetic energy are shown in the bottom row of Figure 3. In contrast with the other variables shown in this figure, TKE is not directly driven by input data and is instead the result of the turbulent energy cascade as resolved by the microscale simulations. It can be observed in all microscale simulations that the daytime boundary layer contains high levels of turbulence, and that after sunset turbulence levels decrease rapidly. Comparison with observed TKE is only possible up to 200 m and suggests that the simulations driven by observations underpredict TKE. We further note that case An shows some regions of high TKE above the boundary layer toward the end of the simulation, and we expect that these might be numerical artifacts. Finally, there appears to be an episode of very strong turbulence intensity between 0600 and 1200 UTC near the top of the TTU tower, but this is not predicted by any of the microscale simulations. Detailed analysis of the measurements data (not shown) revealed that the two highest stations of the TTU meteorological tower measured excessively high turbulence levels between 0600 and 1200 UTC as compared to both lower measurement stations and earlier times. The timing of these suspicious measurements concurs with the formation of the observed LLJ (see also Figure 6l), and we believe that the extreme reported variance likely is a measurement error due to excessive vibrations of the sonic boom arm caused by high wind loading.

To obtain a more quantitative view on the temporal evolution, we now look at the time history of the flow at hub height (Figure 4) and in the surface layer (Figure 5).

Figure 4 shows the wind speed, wind direction, virtual potential temperature, and turbulent kinetic energy at a hub height of 90 m, which is representative for newly installed onshore wind turbines.[45] In terms of wind speed and wind direction (Figure 4A,B), there is a clear distinction between the cases driven by observations (case A0, A1 and An) and case R driven by a mesoscale model. By design of the profile-assimilation technique, case R closely follows the mesoscale simulation and therefore only agrees with the observations when the mesoscale input data correctly predict the wind speed evolution. By contrast, cases A0, A1, and An show much better agreement with the TTU tower wind speed and wind direction because these cases were driven by the observations. The differences among cases A0, A1, and An due to the various θ_v-forcing

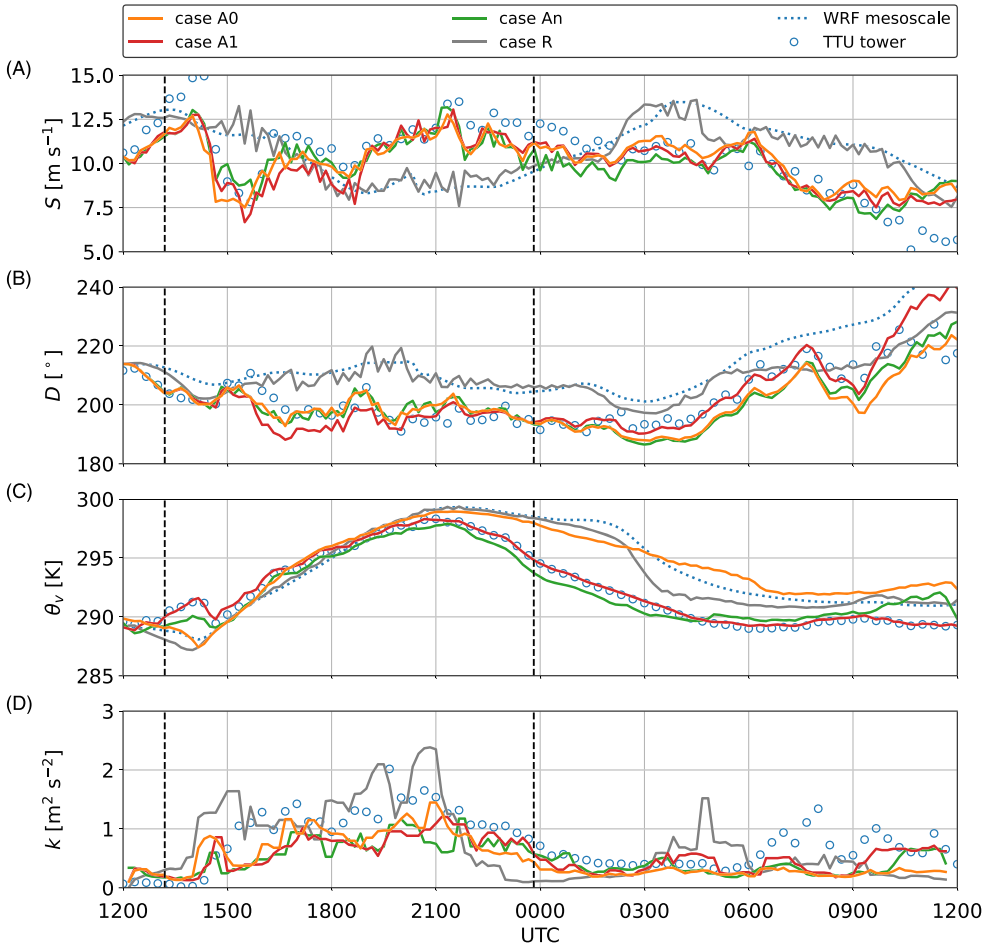

FIGURE 4 Time history of flow quantities at a height of 90 m, including (A) horizontal wind speed S, (B) wind direction D, (C) virtual potential temperature θ_v, and (D) turbulent kinetic energy k, for microscale simulations A0, A1, An, and R. Data from the TTU meteorological tower and from a WRF mesoscale simulation are shown for reference. Simulation and measurement data correspond to 10-min averages, and an additional filter (median value over a rolling window of 30 min) is applied to the TKE. Sunrise and sunset are indicated with vertical dashed lines.

approaches turn out to be small compared to the diurnal variability of the wind speed and wind direction. Note that neither observation-driven nor mesoscale-driven microscale solutions match the input velocity profiles exactly because we use the IPA algorithm, which allows for some deviations from the input profiles to cope with inaccuracies in said profiles (A20). In the last three hours of the simulation, however, cases A0/1/n fail to capture the continued decrease observed in the wind speed, resulting in a relatively large discrepancy between the simulations and observations. The reason for this behavior is not entirely clear and requires more research.

The diurnal evolution of virtual potential temperature in Figure 4C is captured reasonably well by all microscale simulations until 2100 UTC (about 3 h before sunset), after which the results of the various simulations start to diverge. Interestingly, case A0, which assumes that large-scale forcing of virtual potential temperature is negligible, aligns well with case R and with the mesoscale prediction and underpredicts the rate of potential temperature decrease after 2100 UTC as compared to observations from the TTU tower. On the other hand, cases A1 and An, which include some form of θ_v-forcing, are able to follow the observed virtual potential temperature decrease. This seems to suggest that there is a large-scale process at play during the afternoon/evening transition that is not captured by the mesoscale model, but the impact of this large-scale process on the microscale flow can be accounted for by assimilating the observed time–height history of mean virtual potential temperature.

To conclude, the time history of TKE in Figure 4D shows that the various microscale simulations agree reasonably well with the TTU tower observations, capturing both the high levels of turbulence during the daytime and the low TKE levels at night. However, taking a closer look at the last two hours before sunset does indicate that the rate of turbulent decay during the afternoon transition as predicted by the microscale simulations is faster and starts earlier than what is observed by the TTU tower. Moreover, after 0600 UTC observed turbulence levels appear to be somewhat elevated compared to the hours before, which could signal intermittent turbulence. This is not well-represented in any of the simulations.

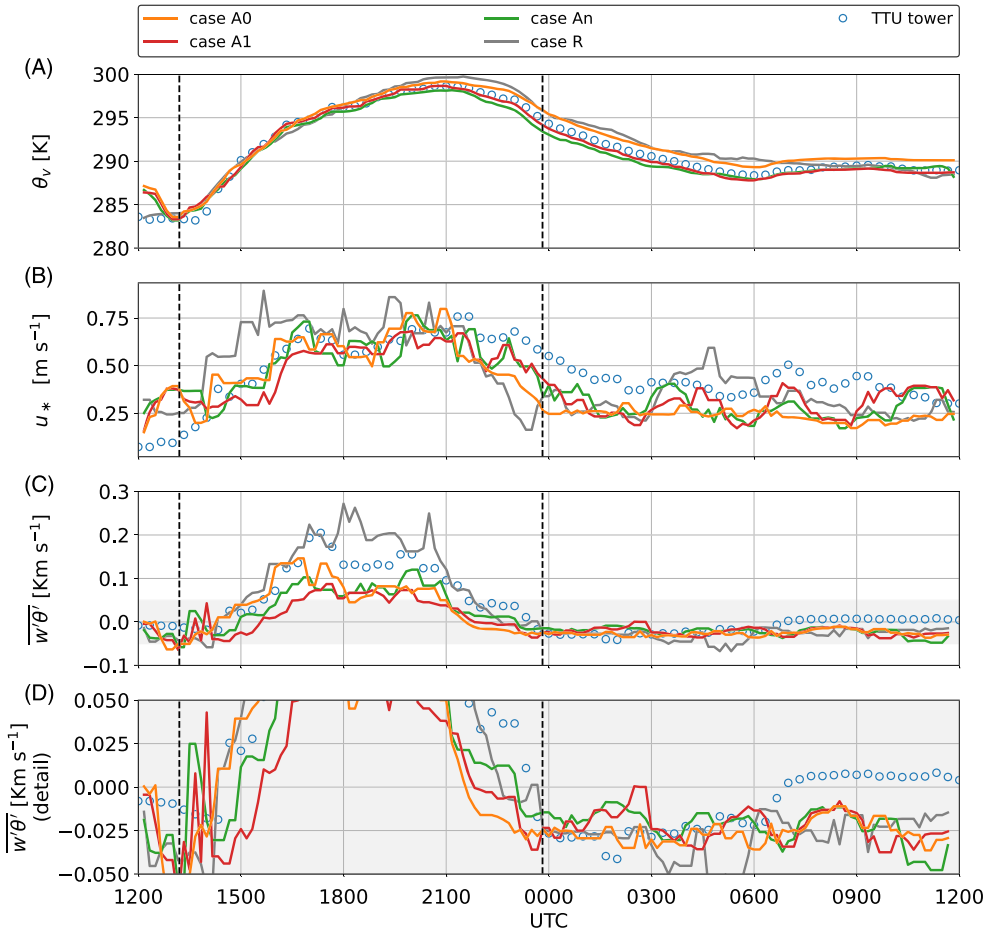

FIGURE 5 Time history of surface-layer quantities, including (A) virtual potential temperature θ_v at 10 m, (B) friction velocity u_*, and (C) surface layer heat flux $\overline{w'\theta'}$. Microscale simulation results for cases A0, A1, An, and R are compared with data from the TTU meteorological tower. Simulation and measurement data correspond to 10-min averages, and an additional filter (median value over a rolling window of 30 min) is applied to the friction velocity and the heat flux. Subfigure (D) shows a detailed view of the surface heat flux (corresponding to the gray area in subfigure (C)) to highlight the differences during the afternoon/evening transition and at night. Sunrise and sunset are indicated with vertical dashed lines.

Figure 5 shows the time history for quantities of interest in the surface layer, including the virtual potential temperature at 10 m, the friction velocity, and the heat flux. The magnitude of the friction velocity and the surface layer heat flux is taken to be the maximum value attained in the surface layer (not necessarily occurring at the first grid cell or measurement level).

The near-surface temperature is predicted relatively well by all microscale simulations, which contrasts with the differences observed earlier at a height of 90 m (see Figure 4C). We hypothesize that near the surface the heat exchange with the ground dominates the flow behavior, while at higher altitudes other large-scale forces start to play a role.

The friction velocity agrees well with the observations during the daytime (see Figure 5B), while during the afternoon transition (roughly between 2100 and 0000 UTC) all simulations predict too low values. The simulations continue to underpredict the friction velocity throughout the nighttime, although case R does predict a period of high friction velocity between 0300 and 0600 UTC, which could be due to an intermittent burst of turbulence. In terms of surface layer heat flux (Figure 5C,D), cases A0, A1, and An (all driven by observations) underpredict the positive heat flux during the daytime, whereas case R driven by mesoscale model data gives a better match. As can be appreciated from the detailed view in Figure 5D, the evening zero crossing, or the time where the surface heat flux changes sign, is predicted too early by all simulations, and there are also significant differences among the various simulations themselves within a 3-h window. This is somewhat surprising since cases A0, A1, and An are all driven using the same surface boundary condition extracted from observations. We believe this is a result of the interplay between the surface heat flux model and the profile-assimilation technique in the first grid cell.

Finally, we also observe a sudden jump in the observed value of the surface heat flux shortly after 0600 UTC, after which the heat flux becomes positive. None of the simulations is able to capture this behavior, and they all predict a relatively constant, strictly negative heat flux

throughout the night. We hypothesize that the flow may have achieved a stable state in which the mean velocity profile developed enough shear under low turbulence such that it transitioned to a higher turbulent state. This might also explain the elevated turbulence levels after 0600 UTC seen in Figure 4. Such intermittent flow behavior is very hard to simulate with LES, especially at a grid resolution of only 10 m and without a cutting-edge subgrid-scale model. Whether or not this could be solved by increasing the grid resolution or adopting a dynamic subgrid-scale model is a subject for future research.

Overall, the results so far show that LES driven by observations are able to capture the diurnal evolution of flow quantities of wind engineering interest, like wind speed and TKE, with similar or even higher accuracy than traditional mesoscale-model-driven simulations. Most importantly, the use of observations implies that the results are not affected by any bias in the mesoscale model predictions. Surprisingly though, even when using observations to drive LES it remains very challenging to accurately match the timing of the evening zero crossing of the heat flux.

4.1.2 | Vertical structure of the boundary layer

We now turn our attention to the vertical structure of the boundary layer throughout the diurnal cycle. Similar to A20, we consider hourly averaged vertical profiles for three representative times of the day: 1800 UTC, which corresponds to 12 p.m. local time and a daytime convective boundary layer; 2200 UTC, corresponding to 4 p.m. and a neutrally stratified boundary layer during the afternoon transition; and 0600 UTC or 12 a.m. local time, representative for the nighttime stable boundary layer. Figure 6 shows vertical profiles of wind speed, wind direction, virtual potential temperature, and turbulent kinetic energy.

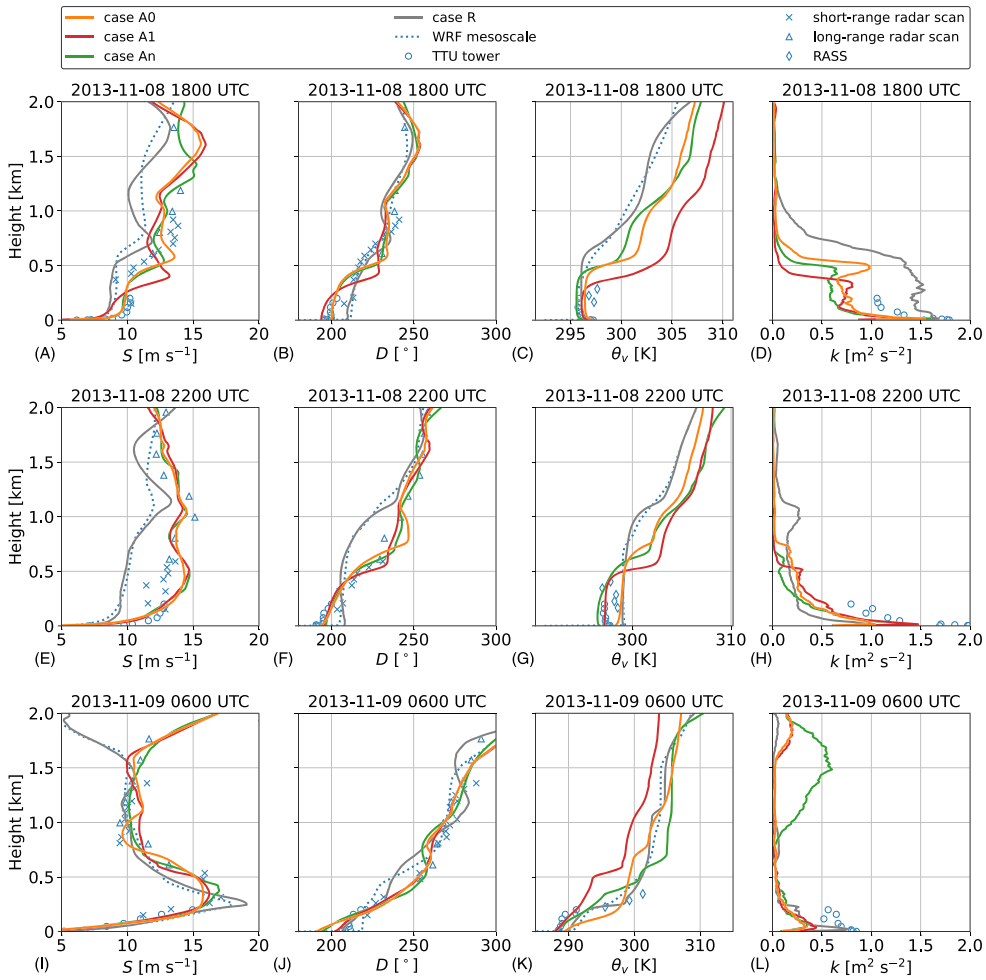

FIGURE 6 Vertical profiles of (A,E,I) horizontal wind speed S, (B,F,J) wind direction D, (C,G,K) virtual potential temperature θ_v, and (D,H,L) turbulent kinetic energy k, averaged over a 1-h period starting at (A–D) 1800 UTC, (E–H) 2200 UTC, and (I–L) 0600 UTC. Microscale simulation results for cases A0, A1, An, and R are compared with data from the TTU meteorological tower, the boundary-layer radar profiler, and a WRF mesoscale simulation.

First, we find that wind speed and direction profiles at 1800 UTC (Figure 6A,B) and especially at 2200 UTC (Figure 6E,F) corroborate our earlier finding that the simulations driven by observed velocity profiles agree well with the tower and radar wind speed, whereas the microscale simulation driven by mesoscale data stays close to the mesoscale prediction itself, resulting in large mean-flow biases. The same holds for the virtual potential temperature profiles in Figure 6C,G, where the results of case R closely follow the mesoscale input data and differ significantly from the other microscale results. At 0600 UTC, the mesoscale prediction of wind speed and direction matches better with the observations, and as a result the microscale simulations agree reasonably well throughout most of the numerical domain (see Figure 6I,J). In the lowest 100 m, all simulations do seem to overpredict the wind veer under stable conditions (Figure 6J).

Next, we jointly analyze vertical profiles of wind speed, wind direction, virtual potential temperature, and turbulent kinetic energy at a particular time. At 1800 UTC, the vertical profiles in Figure 6A–D reveal that some of the differences between the microscale simulations are caused by differences in the boundary layer height (see also Figure 3). The height of the boundary layer can be appreciated in each vertical profile: Near the top of the ABL, wind speed attains a local maximum, wind direction and virtual potential temperature experience a sudden jump, and TKE drops rapidly to zero (similar flow features near the top of the ABL have been observed before in LES of neutral and convective boundary layers[46–48]). Locating these flow features in the various vertical profiles shows that the microscale simulations predict different boundary-layer heights.

At 2200 UTC, similar flow features can be observed in the vertical profiles, although they are often less pronounced than at 1800 UTC. Moreover, while there is still a clear difference between case R and cases A0/1/n, the differences among cases A0/1/n themselves have become small.

At 0600 UTC, the boundary layer is stably stratified, and the vertical structure is quite different from its neutral and convective counterparts. Most notably, an LLJ is present in the wind speed profile. There are, however, some clear differences among the various simulations in terms of the height, width, and strength of the nocturnal LLJ. As already seen qualitatively in Figure 3, both the mesoscale model and the mesoscale-driven case R predict a strong and narrow LLJ relatively close to the ground (jet nose at 245 m), while the observations-driven cases A0, A1, and An predict a broader and weaker LLJ occurring at slightly higher altitudes (jet nose close to 355 m). As explained by Shapiro and Fedorovich[49] and shown for canonical LES of developing stable boundary layers by Allaerts and Meyers,[50] LLJs have greater wind speeds, are more narrow, and occur at lower heights when the reduction in surface layer turbulence levels is larger, corresponding to a stronger frictional decoupling between the stable boundary layer and the residual layer above. As shown in Figure 4D, case R does reveal the strongest reduction in TKE during the evening transition (between 2200 and 0000 UTC), which may explain the difference in jet characteristics observed at 0600 UTC.

At this point, we stress that a detailed validation of the vertical structure of the boundary layer is challenging because of the limited availability and quality of data at the SWiFT site above 200 m. For example, it is very difficult to determine the actual boundary layer height from the observations shown in Figure 6A–D without detailed and reliable measurements of virtual potential temperature and TKE up to the top of the ABL. Consequently, we cannot say which microscale simulation yields the most accurate prediction of the height and vertical structure of the boundary layer. Similarly, the LLJ nose appears to occur above the highest measurement level of the TTU tower and the radar range gate between 150 m and 2000 m is only 60 m. Therefore, we can only very cautiously note that the prediction of a broad and weak LLJ at 350 m aligns better with the available data points.

Finally, in Figure 6L, we notice enhanced levels of TKE near the top of the numerical domain in all microscale simulations, and especially in case An the vertical extent and value of TKE increase is problematic (see also Figure 3). This behavior is clearly unphysical, and we suspect it is caused by the potential temperature profile being close to neutral (i.e., constant with height) rather than stable toward the top of the numerical domain (see Figure 6K). Because of the neutral stratification higher up, turbulence is not damped out and is able to develop freely. The unphysical nature of the potential temperature profiles may be an artifact of the IPA technique and is subject for further research. For example, recent work[30] has shown that the choice of DPA and/or IPA for momentum and temperature forcing can result in drastically different flow fields in the ABL and free atmosphere, corresponding to different resolved turbulence characteristics.

Figure 7 shows the hourly averaged profiles of vertical turbulent flux of momentum and heat, again at 1800 UTC (unstable conditions), 2200 UTC (neutral), and 0600 UTC (stable).

During the daytime (i.e., at 1800 UTC), cases A0/1/n agree well with the observations in terms of the turbulent momentum flux (Figure 7A), while the turbulent heat flux is underestimated (Figure 7D). Case R, on the other hand, overestimates both momentum and heat flux. Further, notice that in these profiles we can also see signs of the boundary layer height—namely, the turbulent momentum flux becomes nearly zero at the top of the boundary layer, and the vertical heat flux attains a local minimum before going to zero. These profiles demonstrate once more that the height of the boundary layer is different among the various simulations. Moreover, it seems that a higher boundary layer leads to larger vertical turbulent fluxes. A possible reason could be that the ABL height limits the largest eddies in size, so a taller boundary layer leads to larger and more energetic eddies and therefore also higher turbulent fluxes.[51] Accordingly, accurately predicting the ABL height might be a necessary condition to achieve good agreement with observations in terms of vertical turbulent fluxes (and possibly also TKE, see Figure 6D). Unfortunately, we cannot validate this statement as we cannot deduce the actual boundary layer height from the available observations.

For the neutral boundary layer at 2200 UTC, cases A1 and An seem to predict the turbulent momentum flux reasonably well, while the predictions of cases A0 and R are slightly too low. The simulation results for the turbulent heat flux, on the other hand, are very different from each other and do not compare well with the observations. The reason for these big differences in the shape of the vertical turbulent heat flux is that

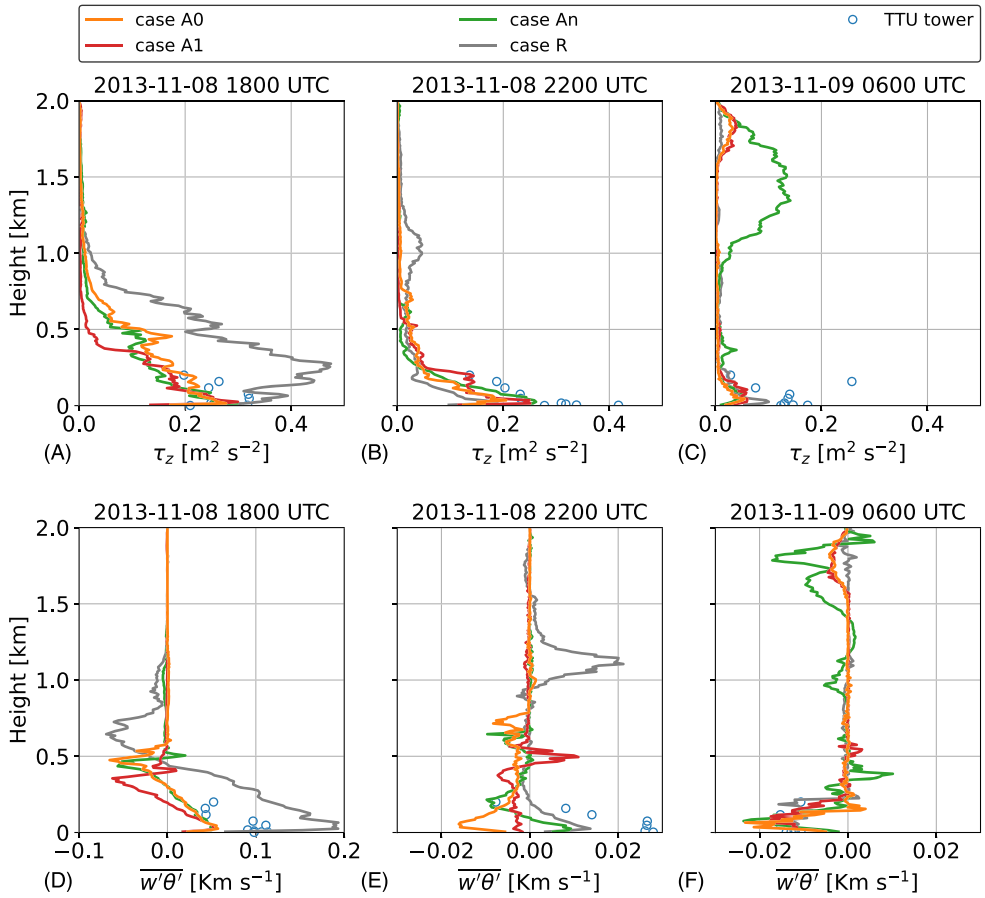

FIGURE 7 Vertical profiles of (A–C) resolved vertical turbulent momentum flux $\tau_z = (\overline{u'w'}^2 + \overline{v'w'}^2)^{0.5}$, and (D–F) resolved vertical turbulent heat flux $\overline{w'\theta'}$, averaged over a 1-h period starting at (A,D) 1800 UTC, (B,E) 2200 UTC, and (C,F) 0600 UTC. Microscale simulation results for cases A0, A1, An, and R are compared with data from the TTU meteorological tower.

the boundary layer is in a transitional state, and the timing of the transition varies among the simulations. For example, the turbulent heat flux of case R and case An still look like convective profiles (positive heat flux near the ground and a local minimum near the top), case A0 already looks like a stable profile (heat flux is negative throughout with a minimum close to the ground), and case A1 is somewhere in between. This is expected given the differences in the evening zero crossings observed earlier in Figure 5D.

At 0600 UTC, all simulations seem to correctly predict the height of the stable boundary layer (the height where the turbulent momentum flux becomes nearly zero). However, the maximum momentum flux near the surface seem to be underestimated by cases A0/1/n. This might be a sign that the LES has difficulties to resolve the stably stratified turbulence with the given grid resolution. The turbulent heat flux, on the other hand, seems to match well with the observations. Further, note again that there appear to be nonzero turbulent fluxes near the top of the domain, especially for case An, and these are related to the enhanced levels of TKE observed in Figure 6L.

In summary, analysis of the vertical structure of the boundary layer shows that the height of the atmospheric boundary layer forms a key flow parameter and influences the vertical profiles of first- and second-order flow statistics. The various forcing approaches lead to different estimates of the boundary-layer height and hence different vertical structures (e.g., LLJ characteristics), but a detailed validation of the boundary layer structure would require more high-quality data above 200 m.

4.1.3 | Turbulence characteristics

The spatial structure of turbulence throughout the diurnal cycle is visualized in Figure 8 by means of instantaneous contours of horizontal wind speed fluctuations in an x–y plane at a height of 120 m for various times of the day.

At 1500 UTC (9 a.m. local time), high- and low-speed velocity streaks dominate the wind field in all simulations, although small differences are observed in terms of magnitude and width of the velocity streaks. Note that, due to the periodicity of the numerical domain, the velocity

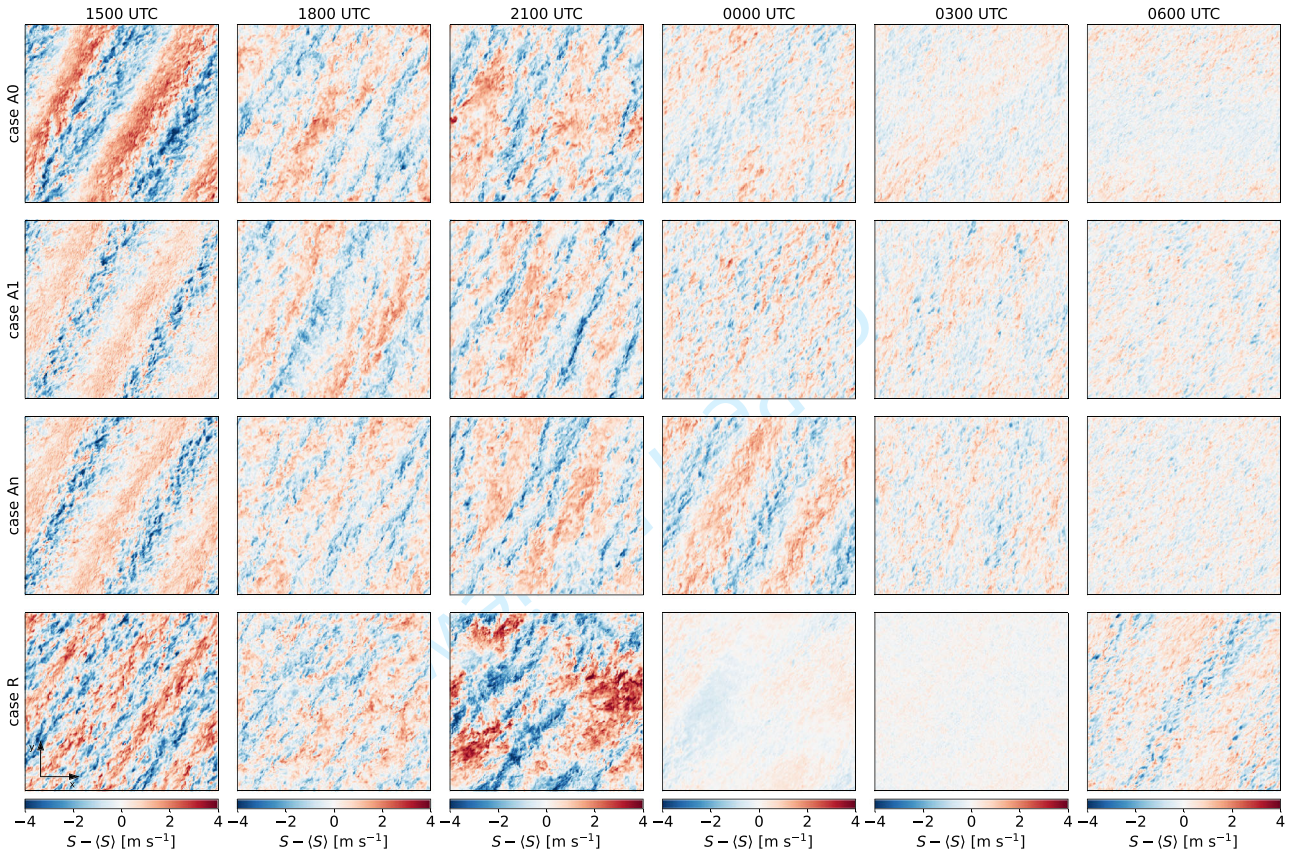

FIGURE 8 Instantaneous contours of horizontal wind speed fluctuations $S - \langle S \rangle$ (with $\langle S \rangle$ the planar-averaged wind speed) in an x–y plane at a height of 120 m; note that the wind is south-southwesterly. Results are shown for cases A0, A1, An, and R (rows) at 1500 UTC, 1800 UTC, 2100 UTC, 0000 UTC, 0300 UTC, and 0600 UTC (columns)

streaks are locked in place, and therefore the spatial coherence in the direction perpendicular to the mean wind direction might be overestimated. As the daytime convective boundary layer evolves, the velocity streaks become less prominent and turbulence is organized in large patches (see contours at 1800 and 2100 UTC). At 2100 UTC, turbulence levels seem significantly higher for case R than for the other cases, in line with earlier findings based on Figure 4D.

In the evening, the boundary layer becomes stably stratified and the intensity and spatial scale of turbulence decreases (see contours at 0000, 0300, and 0600 UTC). Interestingly, cases An and R (to a lesser extent) still show relatively large turbulent structures at 0000 UTC, while the wind fields for cases A1 and A0 only contain small length scales. This indicates that the transition from convective to stable conditions occurs later for cases An and R (see also Figure 5C,D). Finally, we observe that case R predicts a much lower turbulence intensity at 0000 UTC and 0300 UTC than the other cases, and this is again in line with earlier findings (see Figure 4D).

Figure 9 shows the temporal power spectrum over the entire diurnal cycle for horizontal and vertical wind speed, and virtual potential temperature. Following Schalkwijk et al,[14] we show both the raw output of the fast Fourier transform (shaded areas, only shown for case A0 and the TTU tower) and the average over bins of exponentially increasing size. The dashed red line corresponding to a time scale of 10 min serves as a reminder that the input to the LES simulations are 10-min mean values of horizontal wind speed and virtual potential temperature (no vertical velocity).

The power spectra for horizontal and vertical wind speed from all simulations agree remarkably well with the observations for time scales between 10 min and 10 s, both in terms of bin averages and raw data. For time scales below 10 s, the simulated spectra fall-off rapidly as turbulence becomes unresolved, indicating that the effective temporal resolution of the LES is about 10 s (corresponding to an effective LES cut-off frequency of 0.1 Hz). In terms of virtual potential temperature, cases A1 and An again show good agreement, whereas cases A0 and R overpredict the temperature fluctuations at high frequencies. This might be linked to the discrepancy in the evolution of the mean virtual potential temperature (see Figure 4C) due the absence or inaccuracy of θ_v-forcing in cases A0 and R, respectively. For time scales above 10 min, there are some differences between the different simulations, but the overall trends match well with the observations.

Taken together, the results presented in Sections 4.1.1–4.1.3 demonstrate that observational mean-flow data can indeed be used to drive large-eddy simulations. Moreover, while some form of θ_v forcing can improve the prediction of the virtual potential temperature during the

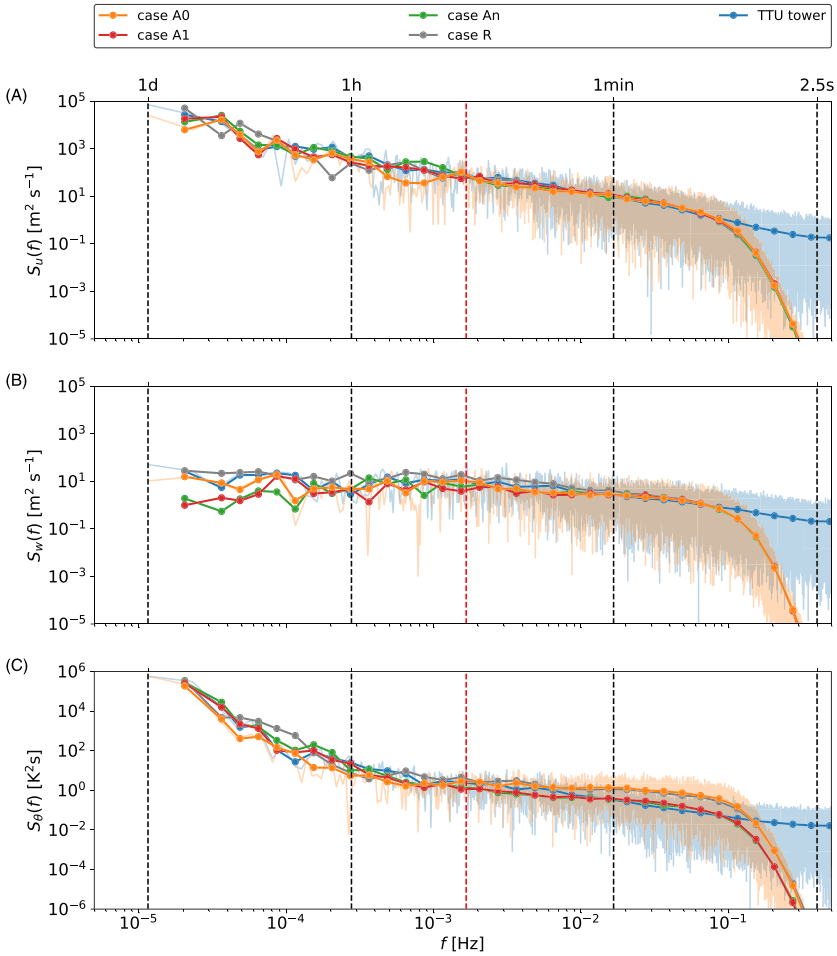

FIGURE 9 Power spectra of (A) horizontal wind speed, (B) vertical wind speed, and (C) virtual potential temperature fluctuations for the full diurnal cycle at a height of 75 m. Microscale simulation results for cases A0, A1, An, and R are compared with the spectra measured by the TTU meteorological tower (using the closest vertical level available, 74.7 m). The shaded areas represent the raw power spectrum of case A0 (orange) and the TTU tower (blue); the lines show the average over bins of exponentially increasing size. The dashed red line corresponds to a time scale of 10 min, which was the input data rate for the LES simulations.

afternoon/evening transition, correctly capturing this behavior does not seem to have a large impact on the wind speed and turbulence at hub height. Therefore, and also because of the issue of enhanced TKE building up near the top of the numerical domain in case An, we use case A0 as our base case in the following sections.

4.2 | Direct versus indirect profile assimilation

This section addresses the second research question as to whether direct profile assimilation can be used in combination with observations. To this end, we compare the results of simulation set B with case A0.

Figure 10 shows the time history of the horizontal wind speed and the turbulent kinetic energy at a height of 90 m (similar to Figure 4).

As expected with DPA, the 10-min averaged horizontal wind speed for cases B0/1/n follows the observations more closely than for case A0. This is particularly true during the daytime—see, for example, the underprediction by case A0 between 1200 and 1500 UTC or during the last hour before sunset. However, these cases also show high-frequency oscillations in the wind speed, and particularly after sunset these oscillation start to acquire seemingly unphysical amplitudes. Note that the results of cases B0/1/n do not match the TTU tower data exactly, as the data in Figure 10 correspond to a single location in the microscale domain, whereas DPA enforces the horizontally averaged wind speed to match the input profiles.

Figure 10B shows that cases B0/1/n all experience episodes of unphysically high TKE, and the issue seems even worse than what was found in A20 (see their Figure 1). Surprisingly, there is one episode during convective conditions (between 1600 UTC and 1900 UTC) for which the

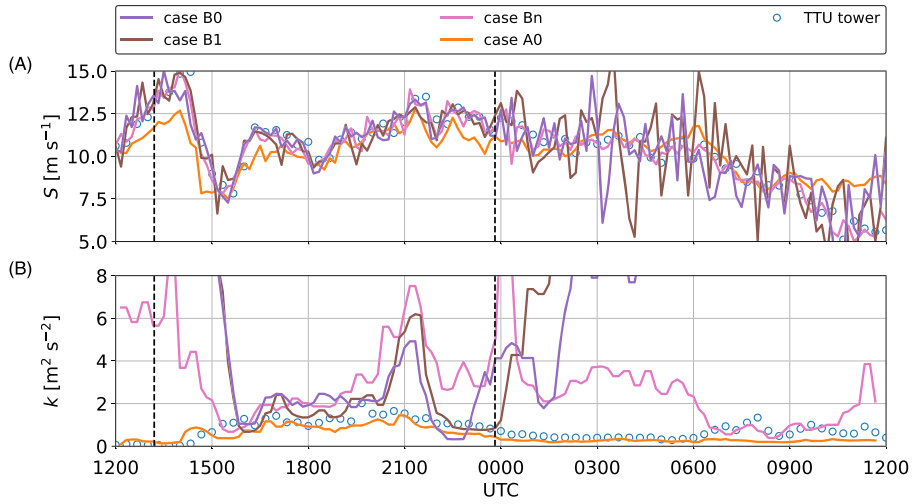

FIGURE 10 Time history of (A) horizontal wind speed S and (B) turbulent kinetic energy k, at a height of 90 m. Microscale simulation results for cases B0, B1, Bn, and A0 are compared with data from the TTU meteorological tower. Simulation and measurement data correspond to 10-min averages, and an additional filter (median value over a rolling window of 30 min) is applied to the TKE. Sunrise and sunset are indicated with vertical dashed lines.

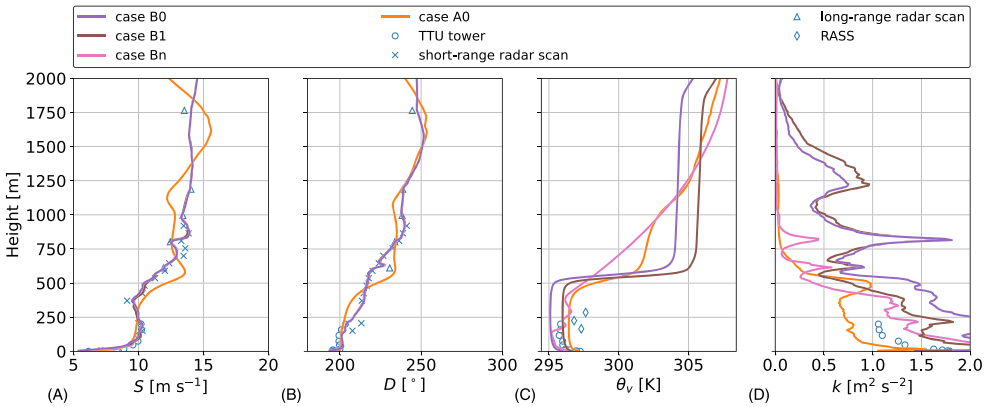

FIGURE 11 Vertical profiles of (A) horizontal wind speed S, (B) wind direction D, (C) virtual potential temperature θ_v, and (d) turbulent kinetic energy k, averaged over a 1-h period starting at 1800 UTC. Microscale simulation results for cases B0, B1, Bn, and A0 are compared with data from the TTU meteorological tower and from the boundary-layer radar profiler.

predictions of TKE for cases B0/1/n are not that far off from the observations. Moreover, it seems that case Bn is not as bad as cases B0 and B1, for which the TKE predictions are even more unrealistic.

To gain some insight into why DPA fails to predict realistic levels of turbulence, Figure 11 shows vertical profiles of hourly averaged flow quantities at 1800 UTC (similar to Figure 6).

In Figure 11A,B, we can see that the wind speed and wind direction predictions very closely match the available observations, leading to "jittery" profiles with fine details compared to the smooth vertical profile of case A0. From past experience with DPA (A20), we know that strictly enforcing velocity profiles can lead to overproduction of turbulence. Additionally, we lack reliable observations to maintain a realistic virtual potential temperature profile. As can be seen in Figure 11C, the high levels of turbulence have led to well-mixed layers both below and above the very stable inversion layer in cases B0 and B1, for which the θ_v-forcing is either zero or constant with height. As the layer above the boundary layer is no longer stably stratified, turbulence is no longer suppressed by stability and can develop freely, as can be appreciated in Figure 11D. At later times, the inversion layer completely disappears and the well-mixed layer extends to the top of the domain (not shown), explaining the extremely large TKE values for cases B0 and B1.

Case Bn, on the other hand, does have height-dependent forcing to enforce a more realistic virtual potential temperature profile, and this results in a reasonable TKE profile at 1800 UTC (see Figure 11D). At later times, however, the stratification only partly succeeds in damping out

excessive turbulence, which explains why the TKE in Figure 10B is not as bad as for cases B0 and B1. Furthermore, small inconsistencies between measurements from the tower and RASS lead to a nonuniform virtual potential temperature profile inside the atmospheric boundary layer, and this could also lead to additional unphysical turbulence production.

Finally, the episode of reasonable TKE prediction during convective conditions in Figure 10B might be explained by the fact that at this time of the day the potential temperature profile inside the atmospheric boundary layer is well-mixed, and this is represented well in cases B0/1/n. By matching the measured mean velocity profile in the simulation, it is likely that turbulence production is also well-predicted, leading to reasonable turbulence levels. Therefore, we conclude that DPA with observations might work for some specific conditions during the daytime and below the inversion layer, but in general the approach leads to unphysically high levels of turbulence and is therefore unusable.

4.3 | Combining observations and mesoscale model data to drive LES

We now address the last research question, which is whether incomplete observational data sets can be complemented with mesoscale-model data. In particular, we assess whether the lack of measured virtual potential temperature profiles can be compensated for with mesoscale-model profiles (case Ca) or with physics-based source terms extracted directly from the mesoscale governing equations (case Cb). We compare simulation set C with case A0 (same momentum forcing as cases Ca/b) and with case R (same θ_v-forcing as case Ca).

Figure 12 shows the time history of the various flow quantities at a height of 90 m (similar to Figure 4).

We observe that the results of cases Ca/b are close to those of case A0 and hence compare well with the TTU tower observations in terms of wind speed and wind direction (Figure 12A,B), which is to be expected as these cases share the same momentum forcing approach. Moreover, we find once more that the impact of the θ_v-forcing approach on the wind speed evolution is small. Figure 12C shows that neither case Ca nor Cb is able to correctly predict the rate of potential temperature decrease during the afternoon/evening transition (i.e., after 2100 UTC), and instead the results of both cases are more in line with cases A0 and R, and with the mesoscale data. It turns out that adding mesoscale θ_v-forcing cannot drive the LES results toward the observed potential temperature, which is again to be expected given the difference between the mesoscale

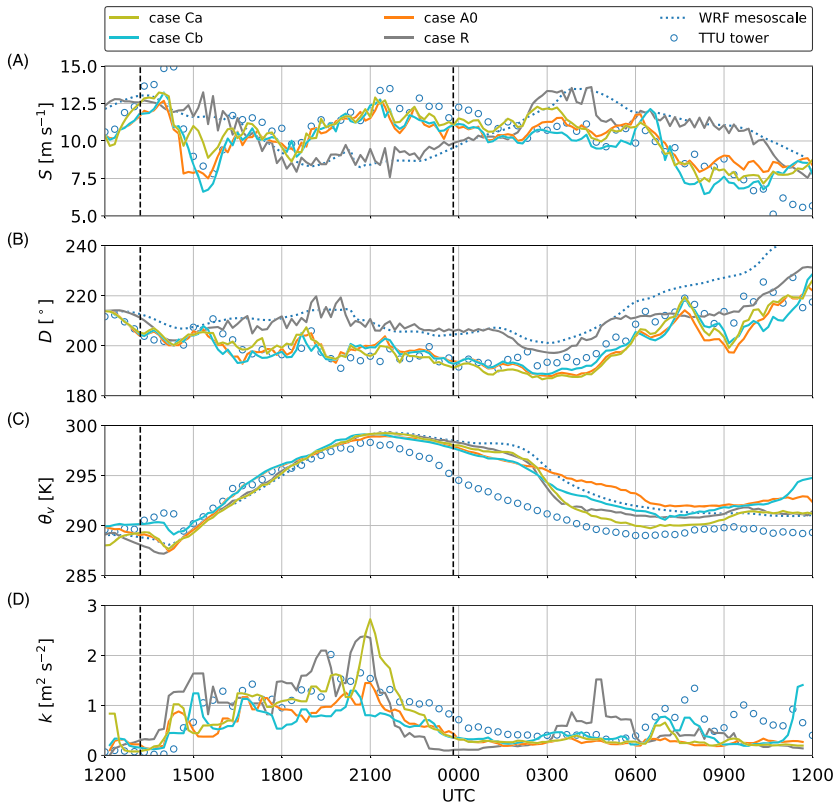

FIGURE 12 Time history of flow quantities at a height of 90 m, including (A) horizontal wind speed *S*, (B) wind direction *D*, (C) virtual potential temperature θ_v, and (D) turbulent kinetic energy *k*, for microscale simulations Ca, Cb, and A0. Data from the TTU meteorological tower and from a WRF mesoscale simulation are shown for reference. Simulation and measurement data correspond to 10-min averages, and an additional filter (median value over a rolling window of 30 min) is applied to the TKE. Sunrise and sunset are indicated with vertical dashed lines.

simulation data and the observed virtual potential temperature evolution. Further, the TKE at hub height predicted by cases Ca/b agrees well with cases A0 and R, and with the observations. The rate of turbulent decay during the afternoon transition in cases Ca/b follows that of case A0 and is too strong compared to the observations. Interestingly, there is a large peak in TKE at about 2100 UTC in cases Ca and R but not in cases Cb and A0. This might be related to the θ_v-forcing approach, which is the same for cases Ca and R.

To further ascertain the adequacy of combining observational and mesoscale driving data, Figure 13 shows vertical profiles of hourly averaged flow quantities at 1800, 2200, and 0600 UTC (similar to Figure 6).

At 1800 UTC, case Ca outperforms all other cases and shows very good agreement with the available observations for all flow quantities, and especially in terms of the TKE profile the agreement is excellent. Case Cb also performs reasonably well, but it is closer to case A0 and underpredicts TKE in the boundary layer. Further, it is interesting to note the differences in boundary-layer height between cases Ca/b and A0 (most noticeable in the potential temperature profile in Figure 13C), which are due to the differences in θ_v-forcing. As expected, case Ca closely follows the mesoscale potential temperature profile (similar to case R), while cases A0 and Cb exhibit stronger inversion strengths and lower inversion heights. This difference in the virtual potential temperature profile also affects the vertical structure of the other flow quantities because the inversion layer controls the top of the boundary layer. This finding demonstrates once more that IPA drives the microscale mean flow toward the specified input profile, but at the same time it allows the atmospheric boundary layer to interact with said profiles and find its own equilibrium.

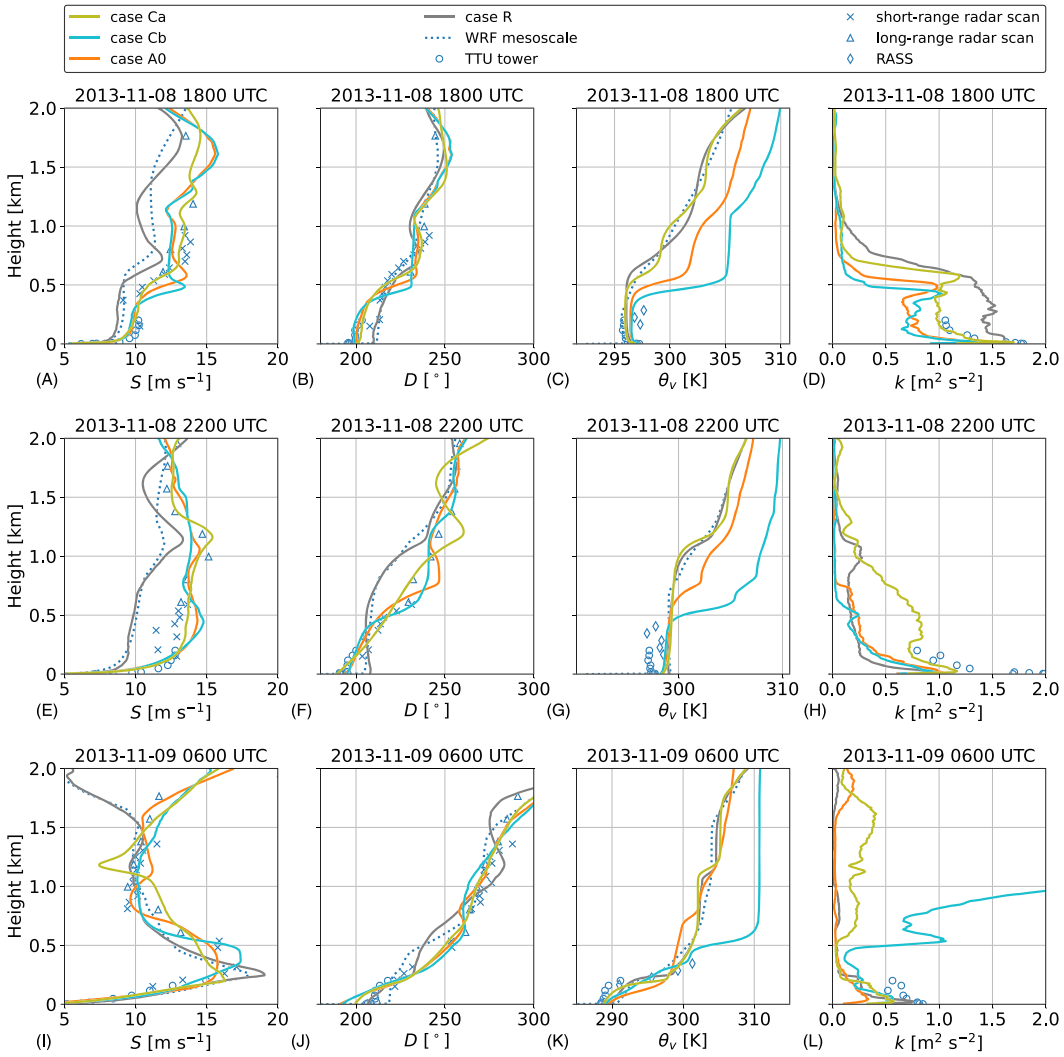

FIGURE 13 Vertical profiles of (A,E,I) horizontal wind speed S, (B,F,J) wind direction D, (C,G,K) virtual potential temperature θ_v, and (D,H,L) turbulent kinetic energy k, averaged over a 1-h period starting at (A–D) 1800 UTC, (E–H) 2200 UTC, and (I–L) 0600 UTC. Microscale simulation results for cases Ca, Cb, and A0 are compared with data from the TTU meteorological tower, the boundary-layer radar profiler, and a WRF mesoscale simulation.

TABLE 2 Mean absolute error (MAE) and normalized MAE (with respect to case R) of rotor-averaged quantities of interest, including the rotor-averaged wind speed S, wind direction D, and turbulent kinetic energy k, the virtual potential temperature difference across the rotor span $\Delta\theta_v$, the wind shear exponent α, and the wind veer ψ (defined as the slope of a linear fit to the wind direction change with height).

	S [$m\ s^{-1}$]		D [$^\circ$]		$\Delta\theta_v$ [K]		k [$m^2\ s^{-2}$]		α [−]		ψ [$^\circ$/100m]	
Name	**MAE**	**NMAE**	**MAE**	**NMAE**	**MAE**	**NMAE**	**MAE**	**NMAE**	**MAE**	**NMAE**	**MAE**	**NMAE**
A0	0.88	0.43	4.41	0.62	2.07	1.55	0.55	0.83	0.14	1.19	13.1	2.05
A1	0.85	0.41	3.64	0.51	0.84	0.62	0.52	0.78	0.10	0.81	7.6	1.19
An	0.91	0.44	4.18	0.59	0.92	0.69	0.53	0.81	0.11	0.93	8.7	1.36
B0	0.92	0.45	3.80	0.53	1.28	0.96	9.63	14.5	0.082	0.67	5.4	0.85
B1	1.14	0.56	4.74	0.67	1.29	0.97	11.3	17.0	0.084	0.69	6.8	1.07
Bn	0.53	0.26	2.11	0.30	0.21	0.16	2.30	3.47	0.067	0.55	3.9	0.61
Ca	0.75	0.36	3.76	0.53	1.67	1.25	0.55	0.83	0.13	1.10	11.1	1.74
Cb	0.93	0.45	4.27	0.60	1.44	1.08	0.53	0.80	0.13	1.11	10.5	1.64
R	2.05		7.12		1.33		0.66		0.12		6.4	

Note: A reference rotor span of 120 m between 30 and 150 m is used.

At 2200 UTC, the boundary layer is much taller in case Ca compared to cases Cb and A0. Moreover, in case Ca the boundary layer contains relatively high levels of TKE up to 1 km, whereas in the other cases the TKE decreases rapidly with height below 500 m. In the lowest 200 m, the TKE prediction in case Ca is only slightly higher than the other cases, and this in fact compares favorably with the observed TKE values.

Finally, at 0600 UTC, the results of case Ca again look reasonable, although residual turbulence levels high above the boundary layer are higher than for case A0. Case Cb, on the other hand, fails to maintain a stably stratified free atmosphere and develops a region of well-mixed potential temperature as shown in Figure 13K (similar to cases B0 and B1, shown for 1800 UTC in Figure 11C), which leads to very high, unphysical levels of turbulence above 500 m. This finding implies that observations and mesoscale data are not always compatible, and combining them to drive microscale simulations does not always work out well.

4.4 | Simulation performance in wind energy terms

The aim of this last section is to give an overall idea on how well the various simulations perform in wind energy terms. To this end, we follow the approach of Sanz Rodrigo et al[28] and compare simulations with observations in terms of rotor-based quantities integrated throughout the diurnal cycle. The quantities of interest are evaluated across a reference rotor region between 30 and 150 m, corresponding to a hub height of 90 m and a rotor diameter of 120 m, and representative of the average newly installed onshore wind turbine in 2020.[45] In addition to the rotor-averaged wind speed, wind direction, and TKE, we also consider the wind shear and wind veer as defined by Sanz Rodrigo et al,[28] and the difference in virtual potential temperature across the rotor span. Simulation performance is evaluated in terms of the mean absolute error (MAE) and the normalized MAE (NMAE), which is obtained by dividing with respect to the MAE of the reference simulation case R. The overall performance metrics are shown in Table 2.

All microscale simulations driven by observations (simulation sets A, B, and C) show a clear improvement in terms of wind speed and wind direction error over case R, which depends on mesoscale model data and hence inherits the bias in the mesoscale prediction. Further, we observe that adding θ_v-forcing (e.g., comparing A1/n and Ca/b with A0) not only affects the virtual potential temperature profile but also leads to small variations in the velocity profile and the turbulence production. In terms of the virtual potential temperature difference across the rotor region, adding θ_v-forcing in cases A1 and An significantly reduces the MAE compared to case A0, and these cases also outperform the reference simulation case R. The performance of cases Ca/b is similar to case R, which is to be expected as these three cases depend on the mesoscale model for information on the θ_v-forcing.

The MAE in turbulent kinetic energy clearly shows that simulation set B is far off from the observed turbulence levels, making the forcing approach based on DPA for this particular site and day unusable. Simulation sets A and C, on the other hand, succeed quite well in predicting correct turbulence levels, and these cases have an MAE which is about 20% lower than for case R. Further, the MAE in terms of shear for sets A and C is comparable to case R, and the prediction of veer is slightly less accurate. This is likely due to an overprediction of the wind veer during stable conditions (see Figure 6J). The prediction of wind shear and wind veer improves slightly by adding θ_v-forcing (compare cases A1/n with A0).

5 | CONCLUSIONS AND OUTLOOK

The aim of this work was to reproduce observed turbulent wind conditions in a doubly periodic large-eddy simulation solely based on single-point observations of the mean flow evolution with height. The time–height-varying large-scale forcing terms required to drive the LES were estimated with the profile-assimilation technique given 10-min mean values of horizontal wind speed and virtual potential temperature up to a height of 2 km above the surface. Unlike other approaches found in literature, the main approach followed in this work did not require an extensive wind profiler or radiosonde network, nor did it depend on an auxiliary mesoscale simulation.

The simulation approach was evaluated for a particular diurnal cycle observed over the SWiFT site in West Texas. The time–height history of wind speed was readily obtained by combining measurements from the TTU meteorological tower and a nearby radar profiler. For the virtual potential temperature, however, the combination of meteorological tower, RASS profiler and radiosonde observations still resulted in extensive data gaps. To cope with the limited availability and the uncertainty in the virtual potential temperature measurements, a suite of nine large-eddy simulations was performed using various approaches for the large-scale virtual potential temperature forcing.

This work's primary finding is that it is indeed possible to drive LES with observational mean-flow data to reproduce the unsteady three-dimensional flow fields with fully resolved turbulence for the various flow regimes occurring throughout a diurnal cycle. Even without applying any large-scale virtual potential temperature forcing, simulations using indirect profile assimilation compared well with observations in term of wind speed, wind direction, and TKE. Moreover, realistic turbulent structures and a turbulent spectrum in good agreement with observations were obtained, proving that LES can generate lifelike atmospheric turbulence corresponding to given mean-flow profiles. The second main finding is that our approach better tracks observations than the traditional mesoscale-model-driven approach. The reason is that, as our approach takes observations as input, it is not susceptible to wind speed biases present in mesoscale model data. We also found that adding θ_v-forcing was

needed to accurately predict the virtual potential temperature near hub height during the afternoon/evening transition, and this also favorably affected wind speed related quantities like wind shear, wind veer, and TKE. To our surprise, correctly predicting the timing of the afternoon/evening transition and the zero crossing of the heat flux turned out to be challenging, and using observations as input did not guarantee a good match. As the timing of the evening transition affects the entire boundary-layer structure around sunset, further research into this aspect is warranted.

We also evaluated the applicability of direct profile assimilation in combination with observations as input. Previous research (A20) showed that DPA in the traditional MMC setting leads to excessive turbulence generation due to inaccuracies in the input mesoscale profiles, so we anticipated better results with observed profiles. Unfortunately, this was not the case, and all simulation using DPA resulted in unphysically high levels of turbulence. Interestingly, though, adding height-dependent θ_v-forcing brought down the turbulence levels to some extent, and realistic results were obtained during a short period of convective, well-mixed conditions inside the boundary layer. We hypothesize that using DPA in combination with observations might be possible, but it would require more accurate measurements of virtual potential temperature throughout the entire boundary layer to allow more reliable θ_v-forcing to keep the DPA momentum forcing and turbulence generation in balance.

Further, we found that using mesoscale data to fill gaps in incomplete virtual potential temperature data was partially successful. Obviously, this approach inherits mesoscale biases in the virtual potential temperature, but it does lead to realistic vertical boundary-layer structures in the microscale. However, the combination of observed profiles and mesoscale budget components resulted in unrealistic profiles of virtual potential temperature and TKE aloft at night. Therefore, combining mesoscale and observational data should be done with care as these two data sources might not always be compatible.

In this work, we considered one specific quiescent diurnal cycle over flat terrain, so our conclusions only hold for this particular case and site. More research is needed to understand how well the proposed approach works at other sites or in more complex synoptic conditions. Furthermore, applying DPA with observations did not work for us, but it did seem to give reasonable results in some other cases.[29] The methodology should be investigated further to understand when and why DPA works. Similarly, IPA worked reasonably well for our case, but the vertical structure of the forcing is rather arbitrary and is known to cause issues near the domain edges, so more research is needed. Finally, despite having access to data from a 200-m meteorological tower, a wind profiler and a radar acoustic sounding system, validation at altitudes above 200 m was limited due to the lack of high-quality data. Especially potential temperature measurements were often lacking and did not reach up high enough. For a thorough validation of the vertical structure of the boundary layer, more high-quality measurements at high altitudes are needed (e.g., from profiling lidars, ceilometers, or Atmospheric Emitted Radiance Interferometers). Similarly, validation of the turbulent fluctuations was limited to the temporal spectrum as the meteorological tower was the only source of high-frequency measurements, so we don't know how well the turbulent structures in the LES compare with reality. Validation of the spatial coherence in the generated turbulence fields, however, would require synchronized measurements at multiple locations, e.g. from scanning lidars or an array of closely spaced meteorological masts.

ACKNOWLEDGEMENTS

The authors thank Patrick Hawbecker and Caroline Draxl for performing the mesoscale WRF simulation and for their help with the radiosonde data, and they also thank Nicholas Hamilton for his data collection and analysis insights. This work was authored in part by the National Renewable Energy Laboratory, operated by Alliance for Sustainable Energy, LLC, for the U.S. Department of Energy (DOE) under Contract No. DE-AC36-08GO28308. Funding provided by the U.S. Department of Energy Office of Energy Efficiency and Renewable Energy Wind Energy Technologies Office. The views expressed in the article do not necessarily represent the views of the DOE or the U.S. Government. The U.S. Government retains and the publisher, by accepting the article for publication, acknowledges that the U.S. Government retains a nonexclusive, paid-up, irrevocable, worldwide license to publish or reproduce the published form of this work, or allow others to do so, for U.S. Government purposes. The research was performed using computational resources sponsored by the Department of Energy's Office of Energy Efficiency and Renewable Energy and located at the National Renewable Energy Laboratory.

DATA AVAILABILITY STATEMENT

The raw data from the meteorological tower[52] and the boundary-layer radar profiler[53] are publicly available on the A2e Data Archive and Portal. The NWS radiosonde data can be downloaded from https://weather.uwyo.edu/upperair/sounding.html. Further, the SOWFA configuration files as well as all python scripts and Jupyter notebooks used for preprocessing and postprocessing of the data are archived under the A2e-MMC GitHub organization (https://github.com/a2e-mmc). Specifically, the configuration files can be found in the "SOWFA-setups" repository (https://github.com/a2e-mmc/SOWFA-setups), while all tools for data pre- and postprocessing can be found in the "assessment" repository (https://github.com/a2e-mmc/assessment). Finally, the SOWFA simulation output of case A0[54] and case R[55] is openly available on 4TU. ResearchData. We decided not to archive the other cases as each case simulates the same diurnal cycle and as not all cases were equally successful. The data from these other cases is available from the corresponding author upon reasonable request.

PEER REVIEW

The peer review history for this article is available at https://publons.com/publon/10.1002/we.2811.

ORCID

Dries Allaerts https://orcid.org/0000-0002-8758-3952

Eliot Quon https://orcid.org/0000-0002-8445-5840

REFERENCES

1. Stull RB. *An Introduction to Boundary Layer Meteorology*. Atmospheric Sciences Library. Kluwer Academic Publishers; 1988.
2. Beare RJ, Macvean MK, Holtslag AAM, et al. An intercomparison of large-eddy simulations of the stable boundary layer. *Bound-Layer Meteorol*. 2006; 118(2):247-272.
3. Sood I, Simon E, Vitsas A, Blockmans B, Larsen GC, Meyers J. Comparison of large eddy simulations against measurements from the Lillgrund offshore wind farm. *Wind Energy Sci*. 2022;7(6):2469-2489.
4. Kumar V, Svensson G, Holtslag AM, Meneveau C, Parlange MB. Impact of surface flux formulations and geostrophic forcing on large-eddy simulations of diurnal atmospheric boundary layer flow. *J Appl Meteorol Climatol*. 2010;49(7):1496-1516.
5. Wang S, Zheng X, Jiang Q. Strongly sheared stratocumulus convection: an observationally based large-eddy simulation study. *Atmospheric Chem Phys*. 2012;12(11):5223-5235.
6. Zhang MH, Lin JL. Constrained variational analysis of sounding data based on column-integrated budgets of mass, heat, moisture, and momentum: approach and application to ARM measurements. *J Atmos Sci*. 1997;54(11):1503-1524.
7. Zhang MH, Lin JL, Cederwall RT, Yio JJ, Xie SC. Objective analysis of ARM IOP data: method and sensitivity. *Monthly Weather Rev*. 2001;129(2): 295-311.
8. Mace GG, Ackerman TP. Assessment of error in synoptic-scale diagnostics derived from wind profiler and radiosonde network data. *Monthly Weather Rev*. 1996;124(7):1521-1534.
9. Casso-Torralba P, Vilà-Guerau de Arellano J, Bosveld F, Soler MR, Vermeulen A, Werner C, Moors E. Diurnal and vertical variability of the sensible heat and carbon dioxide budgets in the atmospheric surface layer. *J Geophys Res: Atmospheres*. 2008;113:D12.
10. Bosveld FC, Baas P, van Meijgaard E, de Bruijn EIF, Steeneveld G-J, Holtslag AAM. The third GABLS intercomparison case for evaluation studies of boundary-layer models. Part A: case selection and set-up. *Bound-Layer Meteorol*. 2014;152(2):133-156.
11. Couvreux F, Guichard F, Redelsperger J-L, Kiemle C, Masson V, Lafore J-P, Flamant C. Water-vapour variability within a convective boundary-layer assessed by large-eddy simulations and IHOP_2002 observations. *Quart J Royal Meteorol Soc*. 2005;131(611):2665-2693.
12. Baas P, Bosveld FC, Lenderink G, van Meijgaard E, Holtslag AM. How to design single-column model experiments for comparison with observed nocturnal low-level jets. *Quart J Royal Meteorol Soc*. 2010;136(648):671-684.
13. Neggers RJ, Siebesma AP, Heus T. Continuous single-column model evaluation at a permanent meteorological supersite. *Bull Am Meteorol Soc*. 2012; 93(9):1389-1400.
14. Schalkwijk J, Jonker HJJ, Siebesma AP, Bosveld FC. A year-long large-eddy simulation of the weather over Cabauw: an overview. *Monthly Weather Rev*. 2015;143(3):828-844.
15. Heinze R, Moseley C, Böske LN, Muppa SK, Maurer V, Raasch S, Stevens B. Evaluation of large-eddy simulations forced with mesoscale model output for a multi-week period during a measurement campaign. *Atmospheric Chem Phys*. 2017;17(11):7083-7109.
16. Sanz Rodrigo J, Allaerts D, Avila M, et al. Results of the GABLS3 diurnal-cycle benchmark for wind energy applications. *J Phys: Confer Ser*. 2017;854: 012037.
17. Sanz Rodrigo J, Arroyo RC, Gancarski P, et al. Comparing meso-micro methodologies for annual wind resource assessment and turbine siting at Cabauw. *J Phys: Confer Ser*. 2018;1037:072030.
18. Olsen BT. Mesoscale to microscale coupling for determining site conditions in complex terrain. *Ph.D. Thesis*. Roskilde, Denmark; 2018.
19. Xie S, Cederwall RT, Zhang M. Developing long-term single-column model/cloud system–resolving model forcing data using numerical weather prediction products constrained by surface and top of the atmosphere observations. *J Geophys Res: Atmospheres*. 2004;109:D1.
20. Xie S, Cederwall RT, Zhang M, Yio JJ. Comparison of SCM and CSRM forcing data derived from the ECMWF model and from objective analysis at the ARM SGP site. *J Geophys Res: Atmospheres*. 2003;108:D16.
21. Conzemius RJ, Fedorovich E. Large eddy simulation of realistic wind fields in daytime atmospheric boundary layer. *Fifth International Symposium on Computational Wind Engineering (CWE2010)*. International Association of Wind Engineering; 2010:8.
22. Gibbs JA, Fedorovich E, van Eijk AMJ. Evaluating weather research and forecasting (WRF) model predictions of turbulent flow parameters in a dry convective boundary layer. *J Appl Meteorol Climatol*. 2011;50(12):2429-2444.
23. Gibbs JA, Fedorovich E. Sensitivity of turbulence statistics in the lower portion of a numerically simulated stable boundary layer to parameters of the Deardorff subgrid turbulence model. *Quart J Royal Meteorol Soc*. 2016;142(698):2205-2213.
24. Zajaczkowski FJ, Haupt SE, Schmehl KJ. A preliminary study of assimilating numerical weather prediction data into computational fluid dynamics models for wind prediction. *J Wind Eng Ind Aerodyn*. 2011;99(4):320-329.
25. Allaerts D, Quon E, Draxl C, Churchfield M. Development of a time-height profile assimilation technique for large-eddy simulation. *Bound-Layer Meteorol*. 2020;176(3):329-348.
26. Stauffer DR, Seaman NL. Use of four-dimensional data assimilation in a limited-area mesoscale model. Part I: experiments with synoptic-scale data. *Monthly Weather Rev*. 1990;118(6):1250-1277.
27. Liu Y, Chen F, Warner T, Basara J. Verification of a mesoscale data-assimilation and forecasting system for the Oklahoma City area during the Joint Urban 2003 field project. *J Appl Meteorol Climatol*. 2006;45(7):912-929.
28. Sanz Rodrigo J, Churchfield M, Kosovic B. A methodology for the design and testing of atmospheric boundary layer models for wind energy applications. *Wind Energy Sci*. 2017;2(1):35-54.
29. Haupt S, Arthur R, Berg L, et al. FY 2020 Report of the Atmosphere to Electrons Land-Based Mesoscale-to-Microscale Coupling Project. PNNL-30841, Richland, Washington, Pacific Northwest National Laboratory; 2020.
30. Jayaraman B, Quon E, Li J, Chatterjee T. Structure of offshore low-level jet turbulence and implications to mesoscale-to-microscale coupling. *J Phys: Confer Ser*. 2022;2265(2):022064.

31. Chatterjee T, Li J, Yellapantula S, Jayaraman B, Quon E. Wind farm response to mesoscale-driven coastal low level jets: a multiscale large eddy simulation study. *J Phys: Confer Ser*. 2022;2265(2):022004.
32. Haupt SE, Kotamarthi R, Feng Y, et al. Second Year Report of the Atmosphere to Electrons Mesoscale to Microscale Coupling Project: Nonstationary Modeling Techniques and Assessment. PNNL-26267, Richland, Washington, Pacific Northwest National Laboratory; 2017.
33. Draxl C, Allaerts D, Quon E, Churchfield M. Coupling Mesoscale Budget Components to Large-Eddy Simulations for Wind-Energy Applications. *Bound-Layer Meteorol*. 2021;179:73-98.
34. Hirth B, Schroeder J. A summary of the National Wind Institute meteorological measurement facilities at the Texas Tech University's Reese Technology Center field site, Lubbock, TX, Texas Tech University; 2014.
35. Kelley CL, Ennis BL. SWiFT site atmospheric characterization. SAND2016-0216, Albuquerque, NM, Sandia National Laboratories; 2016.
36. Skamarock WC, Klemp JB, Dudhia J, et al. A Description of the Advanced Research WRF Version 4. NCAR/TN-556+STR, Boulder, Colorado, National Center for Atmospheric Research; 2019.
37. Haupt SE, Allaerts D, Berg L, et al. FY 2019 Report of the Atmosphere to Electrons Mesoscale-to-Microscale Coupling Project. PNNL-29603, Richland, Washington, Pacific Northwest National Laboratory; 2019.
38. Churchfield MJ, Lee S, Moriarty PJ, Martínez LA, Leonardi S, Vijayakumar G, Brasseur JG. A large-eddy simulation of wind-plant aerodynamics. In: Proceedings of 50th AIAA Aerospace Sciences Meeting. American Institute of Aeronautics and Astronautics; 2012:22.
39. Churchfield MJ, Lee S, Michalakes J, Moriarty PJ. A numerical study of the effects of atmospheric and wake turbulence on wind turbine dynamics. *J Turbulence*. 2012;13:N14.
40. Deardorff JW. Stratocumulus-capped mixed layers derived from a three-dimensional model. *Bound-Layer Meteorol*. 1980;18(4):495-527.
41. Schumann U. Subgrid scale model for finite difference simulations of turbulent flows in plane channels and annuli. *J Comput Phys*. 1975;18(4):376-404.
42. Grötzbach G. Direct numerical and large eddy simulation of turbulent channel flows. In: Cheremisinoff NP, ed. *Encyclopedia of Fluid Mechanics*: Gulf Pub. Co.; 1987:1337-1391.
43. Kosović B, Curry JA. A large eddy simulation study of a quasi-steady, stably stratified atmospheric boundary layer. *J Atmos Sci*. 2000;57(8):1052-1068.
44. Angevine WM, Edwards JM, Lothon M, LeMone MA, Osborne SR. Transition periods in the diurnally-varying atmospheric boundary layer over land. *Bound-Layer Meteorol*. 2020;177(2):205-223.
45. Wiser R, Bolinger M, Hoen B, et al. Land-Based Wind Market Report: 2021 Edition, United States, U.S. Department of Energy; 2021.
46. Pedersen JG, Gryning S-E, Kelly M. On the structure and adjustment of inversion-capped neutral atmospheric boundary-layer flows: Large-eddy simulation study. *Bound-Layer Meteorol*. 2014;153(1):43-62.
47. Allaerts D, Meyers J. Large eddy simulation of a large wind-turbine array in a conventionally neutral atmospheric boundary layer. *Phys Fluids*. 2015;27(6):065108.
48. Allaerts D, Meyers J. Boundary-layer development and gravity waves in conventionally neutral wind farms. *J Fluid Mech*. 2017;814:95-130.
49. Shapiro A, Fedorovich E. Analytical description of a nocturnal low-level jet. *Quart J Royal Meteorol Soc*. 2010;136(650):1255-1262.
50. Allaerts D, Meyers J. Gravity waves and wind-farm efficiency in neutral and stable conditions. *Bound-Layer Meteorol*. 2018;166(2):269-299.
51. Esau IN. Parameterization of a surface drag coefficient in conventionally neutral planetary boundary layer. *Ann Geophys*. 2004;22(10):3353-3362.
52. Atmosphere to Electrons (A2e). mmc/tower.z01.00. 2014. Maintained by A2e Data Archive and Portal for U.S. Department of Energy, Office of Energy Efficiency and Renewable Energy. Date accessed: 16/12/2022. doi:10.21947/1329252
53. Atmosphere to Electrons (A2e). mmc/radar.z01.00. 2014. Maintained by A2e Data Archive and Portal for U.S. Department of Energy, Office of Energy Efficiency and Renewable Energy. Date accessed: 16/12/2022. doi:10.21947/1329730
54. Allaerts D, Quon E, Churchfield M. LES dataset of the 8-9 November 2013 diurnal cycle at the SWiFT site internal.ipa.obs.noT. 4TU.ResearchData; 2023. doi:10.4121/22006592
55. Allaerts D, Quon E, Churchfield M. LES dataset of the 8-9 November 2013 diurnal cycle at the SWiFT site internal.ipa.wrf. 4TU.ResearchData; 2023. doi:10.4121/22014659

How to cite this article: Allaerts D, Quon E, Churchfield M. Using observational mean-flow data to drive large-eddy simulations of a diurnal cycle at the SWiFT site. *Wind Energy*. 2023;26(5):469-492. doi:10.1002/we.2811

APPENDIX A: WRF Model Setup

We used Advanced Research WRF,[36] version 4.1 for this study. The simulation was initialized from 8 November 2013 at 00:00 UTC, 12h prior to the study period. Initial and boundary conditions are provided by the National Centers for Environmental Prediction's Global Forecast System (GFS) model. No large-scale atmospheric nudging was performed. Three nested domains were simulated, centered on the SWiFT site. Additional model parameters are described in Table A1.

TABLE A1 WRF model configuration.

Model feature	Specification
Grid spacing for nested domains (km)	27, 9, 3
Vertical levels	88
Near-surface-level heights (m)	4.8, 9.6, 14.4, 19.2, 24.0, 29.1, 34.4, 39.9, 45.8, 51.9
Large-scale atmospheric forcing	GFS final analysis
Planetary boundary layer scheme	Mellor-Yamada Nakanishi and Niino Level 2.5 (MYNN)
Surface-layer scheme	MYNN
Land surface model	Noah
Microphysics	Morrison double-moment scheme
Longwave radiation	Rapid Radiative Transfer Model for General Circulation Model applications (RRTMG)
Shortwave radiation	RRTMG
Cumulus parameterization	Kain–Fritsch
Topographic database	Global Multi-resolution Terrain Elevation Data 2010, 30-arc-sec data set
Land-use data	Moderate-resolution Imaging Spectroradiometer, 21 category